3 Design Drivers for WIMP Identification

Having established the motivation to perform direct searches for WIMP dark matter, we introduced in the previous section the proposed configuration of LZ. Searching for events that are rare ($\lesssim$0.1 per day per tonne of target mass) and that involve very small energy transfers ($\lesssim$100 keV) is extremely challenging. This section focuses on the more salient features of the experiment and the detection medium, and how these will contribute to the identification of a galactic WIMP signal with low systematic uncertainty. The detailed design and its technical implementation are described in later sections; here, we address the key requirements that drive the conceptual design and how we propose to address remaining technical challenges.

3.1 Overview of the Experimental Strategy

Xenon has long been recognized as a very attractive WIMP target material [1-3]. Its high atomic mass provides a good kinematic match to intermediate WIMP masses of O(100 GeV/c^2) and the largest spin-independent scattering cross section among the available detector technologies, as illustrated in Figure 3.1.1. Sensitivity to lighter WIMPs, with masses of O(10 GeV/c^2), can be also be achieved, given the excellent low-energy scintillation and ionization yields in the liquid phase [4]. Xenon contains neither long-lived radioactive isotopes with troublesome decays nor activation products that remain significant after the first few months of underground deployment. It is also sensitive to spin-dependent interactions via the odd-neutron isotopes ^{129}Xe and ^{131}Xe, which account for approximately half of the natural isotopic abundance. If a WIMP discovery were made, the properties of the new particle could be studied by altering the isotopic composition of the target. This broad WIMP sensitivity confers maximum discovery potential to LZ.

The liquid phase is preferred over the gas phase due to its high density (3 g/cm^3) and high scintillation yield, and because its charge quenching of NRs provides a powerful particle ID mechanism. Early experiments such as ZEPLIN-I [5] exploited simple pulse shape discrimination (PSD) of the scintillation

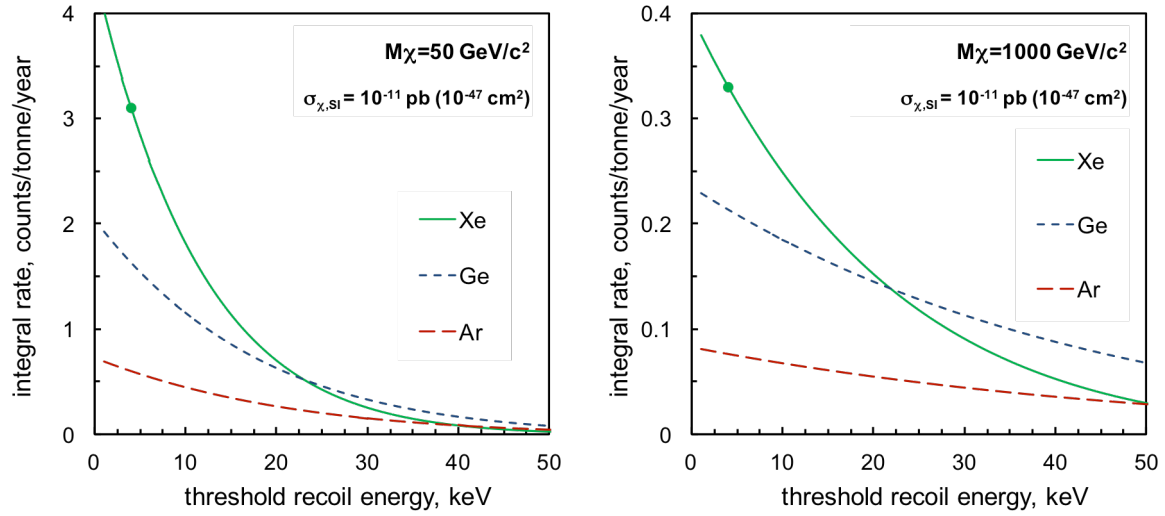

Figure 3.1.1. Integrated rate above threshold per tonne·year of exposure for WIMP elastic scattering on Xe, Ge, and Ar targets for 50 GeV/c^2 and 1 TeV/c^2 WIMP masses and 10^{-47} cm^2 interaction cross section per nucleon. The green marker indicates the 4.3 keV WIMP-search threshold in LUX with nominal ER/NR discrimination [4]. CDMS II searched above 10 keV in their Ge target; selected SuperCDMS detectors allowed a 1.6-keV threshold with lower discrimination [6]. In LAr, the WARP (WIMP Argon Programme) 2.3-liter chamber achieved 55 keV [7], and the DarkSide-50 experiment has recently conducted a WIMP search above 38 keV [8].

signal to reject electronic backgrounds; however, this achieved modest rejection efficiencies and only at relatively high recoil energies. When the first double-phase Xe detectors were deployed for dark-matter searches, in the ZEPLIN-II/III [9,10] and XENON10 [11] experiments, the increase in engineering complexity soon paid off in sensitivity, and this technique has been at the forefront of the field ever since. Comprehensive reviews on the application of the noble liquids to rare-event searches can be found in the literature [12,13].

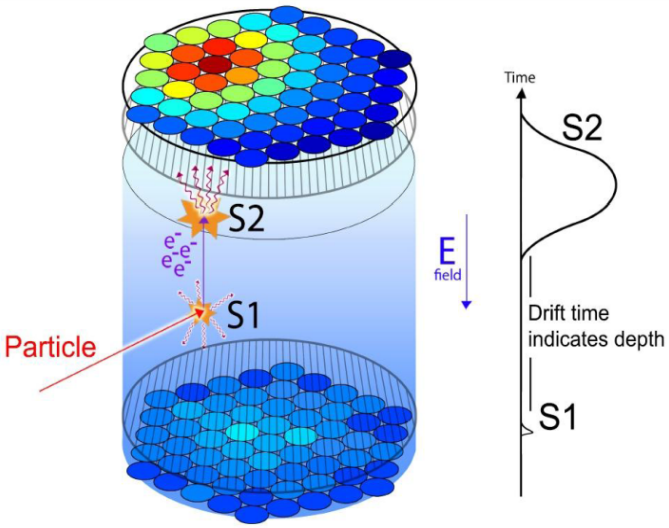

Figure 3.1.2. Operating principle of the double-phase Xe TPC. Each particle interaction in the LXe (the WIMP target) produces two signatures: one from prompt scintillation (S1) and a second, delayed one from ionization, via electroluminescence in the vapor phase (S2). This allows precise vertex location in three dimensions and discrimination between nuclear and electron recoils.

The TPC configuration at the core of double-phase detectors, illustrated in Figure 3.1.2, has several notable advantages for WIMP searches, in that two signatures are detected for every interaction: a prompt scintillation signal (S1) and the delayed ionization response, detected via electroluminescence in a thin gaseous phase above the liquid (S2). These permit precise event localization in three dimensions (to within a few mm [14]) and discrimination between electron and nuclear recoil events (potentially reaching 99.99% rejection [15]).

Both channels are sensitive to very low NR energies. The S2 response enables detection of single ionization electrons extracted from the liquid surface due to the high photon yield that can be achieved with proportional scintillation in the gas [16-18]. In LUX we have demonstrated sufficient S1 light collection to achieve a NR energy threshold below 5 keV [4].

The combination of accurate 3-D imaging capability within a monolithic volume of a readily purifiable, highly self-shielding liquid is nearly an ideal architecture for minimizing backgrounds. It allows optimal exploitation of the powerful attenuation of external gamma rays and neutrons into LXe, distinguishes multiply-scattered backgrounds from single-site signals, and precisely tags events on the surrounding surfaces. This latter feature is important, given the difficulty of achieving contamination-free surfaces. The low surface-to-volume ratio of the large, homogeneous TPC lowers surface backgrounds in comparison to signal, and stands in stark contrast to the high surface-to-volume ratio of segmented detectors.

These concepts are illustrated in Figure 3.1.3, which shows neutron interactions occurring just a few millimeters apart in the ZEPLIN-III detector. The S1 signals are essentially time-coincident, but the S2 pulses have different time delays corresponding to different vertical coordinates, making the rejection of such multiple scatters extremely efficient. The figure shows also a pulse observed in delayed coincidence in the surrounding veto detector, indicating radiative capture of this neutron on the gadolinium-loaded plastic installed around the WIMP target. LZ will utilize a similar anticoincidence detection technique to characterize the radiation environment around the Xe detector and to further reduce backgrounds.

Nevertheless, when the first tonne-scale Xe experiments were proposed just over a decade ago, it was unclear whether LXe technology could be monolithically scaled as now proposed for LZ, or if it would be necessary to replicate smaller devices with target masses of a few hundred kilograms each. The latter option, while conceptually simple, fails to fully exploit the power of self-shielding. Since then, several

aspects of the double-phase TPC technique have been further developed to make LZ technologically feasible. First, the ionization and scintillation yields of LXe and their dependence on energy, electric field, and particle type have now been established down to a few keV by a comprehensive development program carried out around the globe, including substantial work by members of the LZ Collaboration. Second, good acceptance for the primary scintillation light must be maintained as the detector becomes larger, and the remarkably high reflectance (>95%) of PTFE at the 178 nm LXe scintillation wavelength has made this practical. Third, considerable control over electronegative impurities is required to drift charge over a distance of a meter or more, and commercial purification technology and new screening and detection methods developed by LZ scientists have made this routinely achievable. Fourth, the extraordinary self-shielding of an LZ-class instrument requires the use of internal calibration sources, and these have now been developed and deployed within LUX by LZ groups. Fifth, radioactive impurities such as Kr must be reliably removed from the Xe, and other sources of internal radioactivity such as radon must be tightly controlled. Finally, a large detector requires a substantial cathode voltage, or else fluctuations in the charge recombination near the interaction site will degrade the recoil discrimination. Very recently, LUX has demonstrated a rejection efficiency of 99.6% (for 50% NR acceptance) even at a modest field of 180 V/cm [4] — matching already the baseline assumption for LZ. From our present understanding of the physics of recombination, we expect further gains in discrimination at higher fields, and this challenge is a major focus of our current R&D effort.

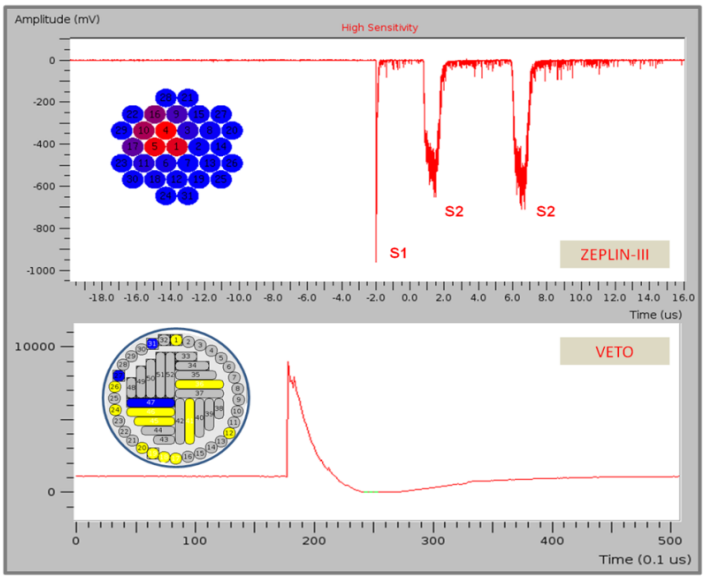

Figure 3.1.3. A double-scatter neutron event recorded in ZEPLIN-III. The upper panel shows two elastic vertices clearly resolved in drift time (two S2 pulses, representing different vertical coordinates), although both have similar horizontal positions. The lower panel shows the summed waveform from the 52-module veto detector which surrounded the main instrument, indicating radiative capture of this neutron some 17 µs after interacting in the LXe target. Recording additional particle scatters (either in the WIMP target or in an ancillary veto detector) provides a powerful rejection of backgrounds.

On the whole, the progressive nature of our program has contributed to an increase in the readiness level of this technology: LZ entails a twentyfold scale-up from LUX, the latter being also an order of magnitude or so larger than the ZEPLIN and XENON10 targets. Besides having the favorable properties of the WIMP target material and the proven sensitivity of the technology to small energy deposits, a successful experiment must achieve very low background rates over a significant fraction of its active medium. Indeed, it is worth noting that LZ will be a factor of 10^4 times more sensitive than current limits from the EDELWEISS and Cryogenic Dark Matter Search (CDMS) experiments, which led in sensitivity only one decade ago [19,20]. This implies a corresponding reduction in the background rate. This is achieved to first order by the power of self-shielding of local radioactivity, in combination with an outer layer of instrumented LXe and a hermetic gadolinium-loaded scintillator "veto" shield capable of tagging neutrons and gamma rays with high efficiency. The construction of a veto instrument at the required scale builds on two decades of development work in the field of reactor neutrino physics, and its development within LZ is led by scientists with considerable expertise in this area. Three other important

developments, again pioneered by LZ groups, have also made this possible: the development, in collaboration with Hamamatsu, of very-low-background PMTs compatible with LXe [21]; the identification via the LUX program of radio-clean titanium for cryostat fabrication [22]; and the development of krypton-removal and -screening technology capable of delivering sub-ppt concentrations [23,24].

This strategy leads to a WIMP-search background of order 1 event in 1,000 days of live exposure for a 5.6-tonne fiducial mass. Remarkably, the remaining component will be due to astrophysical neutrinos, dominated by solar pp neutrino scattering from electrons, with a small fraction of these events mimicking NRs due to the finite S2/S1 discrimination power. Coherent scattering of atmospheric neutrinos from Xe nuclei (CNS) will constitute an even smaller, but irreducible, background. These rates are well understood and background expectations are calculable with small systematic uncertainty (e.g., these events are spatially uniform and their energy spectra are well known). With its pioneering capability, LZ will be sensitive to these ultrarare processes.

3.2 Self-shielding in Liquid Xenon

At the core of any WIMP search experiment is a substantial screening and materials-selection program that controls the trace radioactivity of the detector components. In the case of LZ, however, backgrounds from detector radioactivity will also be rejected to unprecedented levels by the combination of self-shielding of external particles and operation in anticoincidence with outer veto detectors. This will render external gamma rays and neutrons less problematic than in other experiments.

The self-shielding strategy, in particular, relies on the combination of a large, dense, high-*Z* and continuous detection medium with the ability to resolve interaction sites in three dimensions with high precision. An outer layer of the target can therefore be defined (in data analysis) that shields a *fiducial* region with extremely low background at the center of the active medium. The *nonfiducial* layer will be only a few centimeters thick. Because the size of the LZ detector is much larger than the interaction lengths for MeV gamma rays and neutrons, as shown in Figure 3.2.1, when these particles penetrate more than a few cm they will scatter multiple times and be rejected (Figure 3.2.2). X-rays, with energies similar to WIMP events, penetrate only a few mm into the LXe.

Double-phase Xe detectors implement this strategy very successfully, and this is reflected in their present dominance in WIMP sensitivity — with LUX being a prime example of this concept. In LZ, a fiducial mass of nearly 6 tonnes will be practically free of external gamma-ray or neutron backgrounds, which

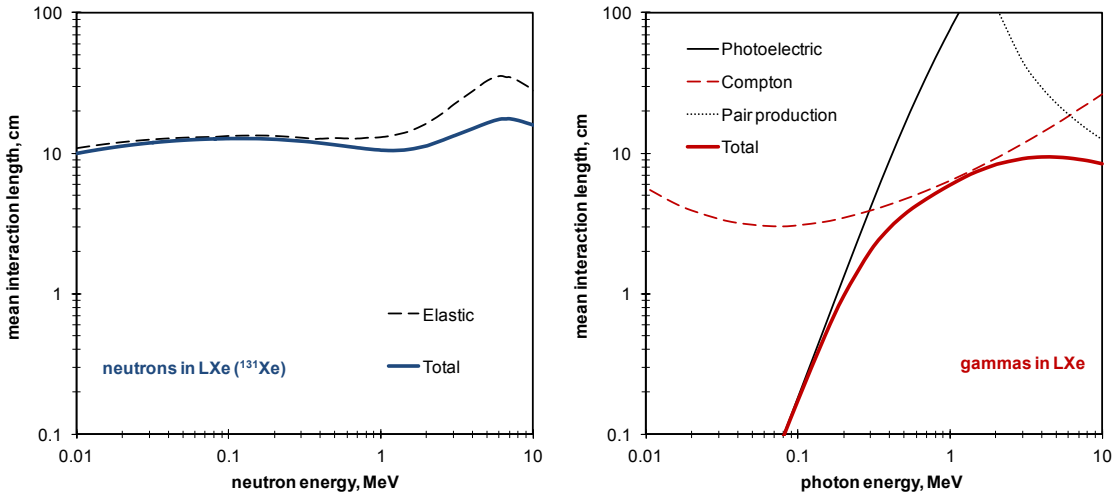

Figure 3.2.1. Mean interaction lengths for neutrons [25] and gamma rays [26] in LXe.

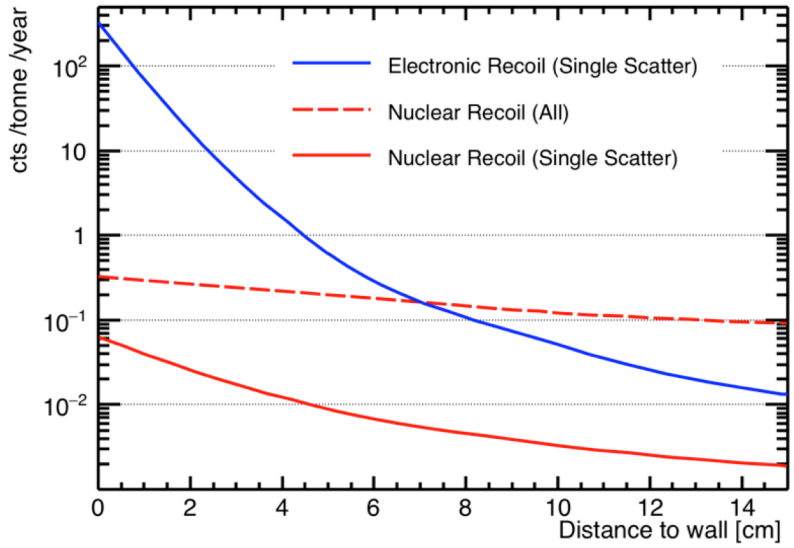

Figure 3.2.2. Self-shielding of external neutrons and gamma rays in LXe. The red lines indicate the number of elastic neutron scatters creating 6–30 keV NRs as a function of distance to the lateral TPC wall; the continuous line shows single scatters only, while the dashed line includes all multiplicities adding up to the same total energy; the input spectrum is that from (α,n) neutron production in PTFE, an important background near the TPC walls. The blue line represents single-site ER interactions from U/Th gamma rays from PTFE with energy 1.5–6.5 keV_{ee}. A tenfold decrease is achieved at ~2 cm and ~6 cm from the wall for gamma rays and neutrons, respectively.

represents 85% of active mass within the TPC, compared to about 50% for LUX [4] and XENON100 [27]. In addition to the required high density and high-*Z* of the detection medium, we highlight the importance of the precise spatial resolution that can be achieved in these detectors, which is of the order of 1 cm or better at threshold. The fiducial fraction can be much smaller in single-phase, scintillation-only detectors, which typically achieve a vertex location of about 10 cm. For example, only (roughly) 5% of the LXe mass was utilized in the recent search for inelastic WIMP scattering in XMASS [28].

3.3 Low-energy Particle Detection in Liquid Xenon

The potential of this medium for particle detection was recognized in the mid-20th century, when the combination of good scintillation and ionization properties was first noted (see [12] and references therein). In the 1970s, the first double-phase detectors were demonstrated, originally using argon [29]. Initially, our understanding of the mechanisms involved in generating the scintillation and ionization responses in the noble liquids progressed slowly, especially regarding the response to low-energy nuclear and electron recoils. However, great steps have been taken in the past decade, with LZ collaborators taking a central role. This effort continues around the world.

In this section, we summarize those LXe properties that affect the detection of low-energy nuclear and electronic recoils via scintillation and ionization; the next section discusses how to discriminate between them. The response of LXe to electron and nuclear recoils is now well understood over the energy range of interest for "standard WIMP" searches (≳3 keV). Significant progress has equally been made in modeling its behavior as a function of incident particle species, energy, and electric field, in order to optimize detector design and the physics analyses. Naturally, the increasing WIMP scattering rates with decreasing recoil energy and the need to probe lighter dark-matter candidates mean that pushing further down in threshold is a perennial concern for any detection technology.

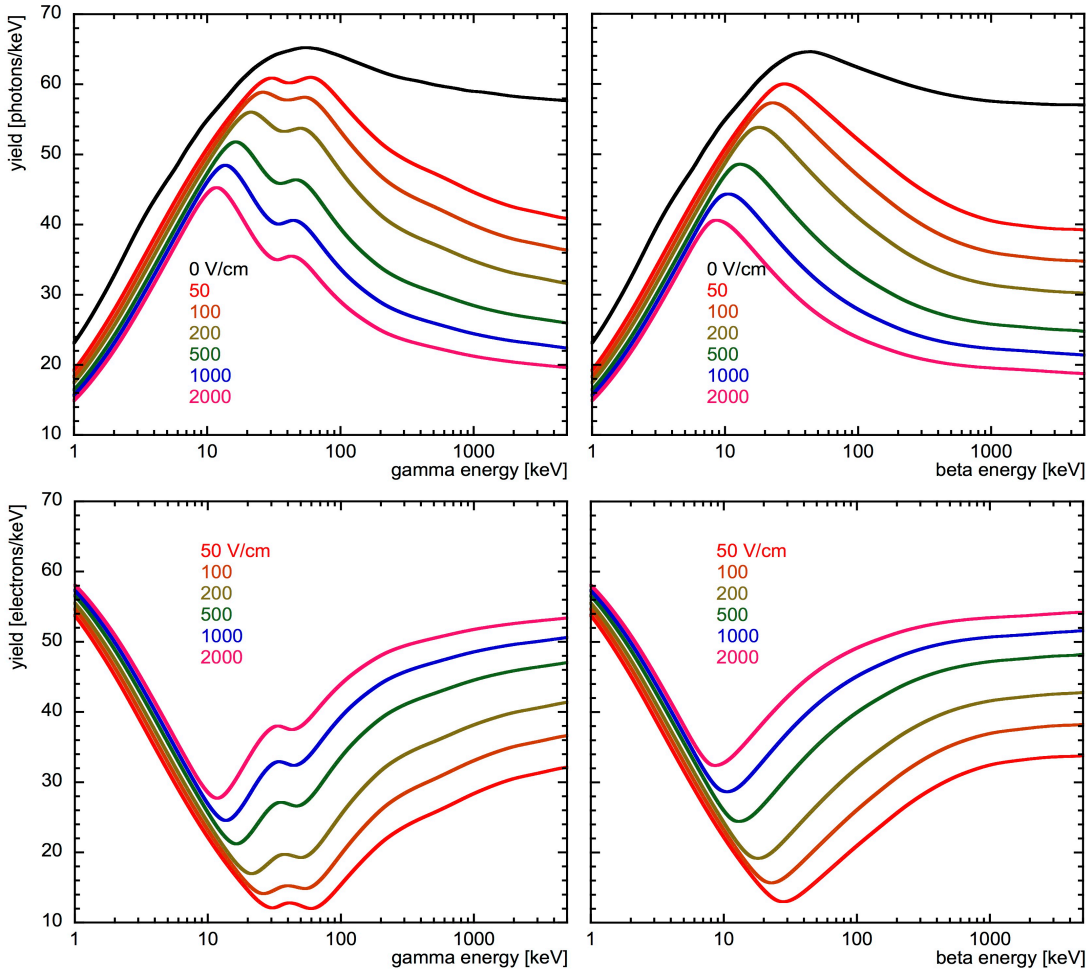

Figure 3.3.1. NEST predictions of light (top) and ionization yields for ERs in LXe, for incident gamma rays (left), and primary electrons (β-particles, δ-rays) (right) [30]. Increasing the electric-field strength reduces recombination, raising the charge yield at the expense of light. The dip in the gamma-ray curves is due to the Xe K-shell X-ray that creates a second interaction site, displaced from the initial energy deposition.

Scintillation and ionization yields for ERs in LXe are shown in Figure 3.3.1, as predicted by the Noble Element Simulation Technique (NEST) model (see [30-32] and the brief description in the next section); data for Compton electrons now reach down to 1.5 keV [31,33], and NEST shows good agreement with these results [34]. LXe compares favorably to the best scintillators and is also a good ionization medium. For example, the maximum photon yield at a few tens of keV is some 40% higher than that of liquid argon. This is important for a number of reasons: It reduces the variance of the ER response, which is important for particle discrimination; it permits effective detector calibration; and it is directly relevant to some leptophilic dark-matter searches.

As Figure 3.3.1 suggests, the scintillation yield is suppressed with increasing electric-field strength, while the ionization yield improves by the same amount. This behavior is also observed for individual events: A fraction of the photon yield comes from recombination luminescence, whereby VUV photons are generated from electron-ion recombination occurring near the interaction site, and therefore some electrons contribute either to scintillation (S1) or to ionization (S2), but not to both. This event-by-event anticorrelation of the two signatures can be exploited very effectively at higher energies in double-phase

detectors to obtain good energy resolution for the spectroscopy of ERs, with application to gamma-ray background studies and searches for 0νββ decay.

For NRs, both data and modeling have progressed markedly in recent years. The picture here is more complex than for electron interactions. Most of the energy deposited by electrons is shared between ionization and excitation of the medium, making much of it observable. In NR interactions, a larger fraction is spent in atomic collisions, which is dissipated as heat and not detected. However, data obtained by scattering experiments at neutron beams ex situ, e.g. [35,36], are now in good agreement with those from indirect in situ techniques [37], down to ~3 keV.

The ability of our models to reproduce these results has also improved, as shown in Figure 3.3.2, which summarizes the scintillation yield from Xe recoils in LXe. As has been the case with ERs, new NR calibration techniques will continue to decrease the uncertainties still affecting the lowest energies; in fact, LUX is pursuing such calibration work. The impact of this remaining uncertainty in the LZ sensitivity predictions is discussed in Chapter 4.

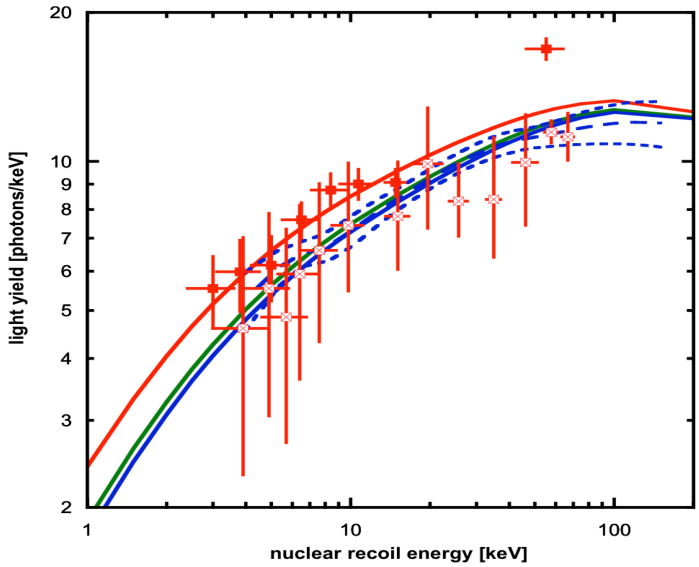

Figure 3.3.2. Absolute NR scintillation yield in LXe. Hollow red markers are from neutron-beam measurements at Yale [35] and filled markers from [36] — both at zero field. Blue dashed lines are the combined mean and 1-σ curves from two in situ measurements with Am-Be neutron sources via fitting to MC simulation from ZEPLIN-III [37] (3,650 V/cm). The NEST model [33] is shown in red, green, and blue for zero field, 700 V/cm (LZ baseline), and 3,650 V/cm, respectively. The green curve conservatively zeroed below 3 keV is used for LZ sensitivity calculations.

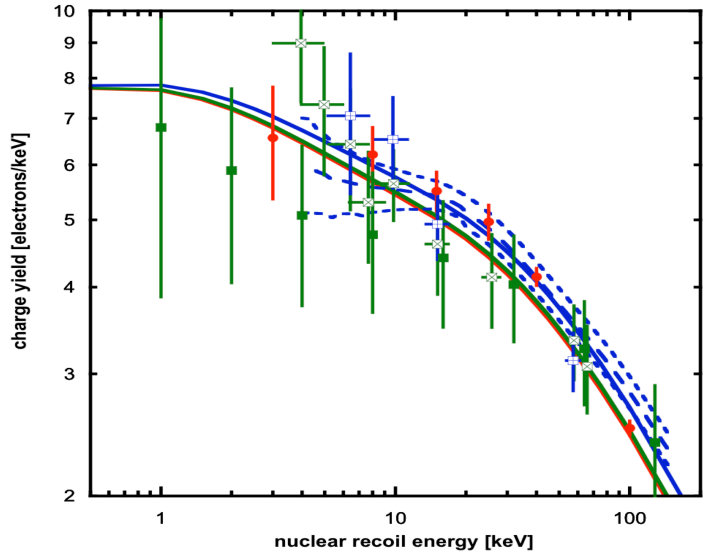

Figure 3.3.3. NR ionization yield in LXe. Data are as follows: blue and green hollow squares from neutron beam data from Yale at 4 kV/cm and 1 kV/cm, respectively [35]; dashed blue curves from Monte Carlo matching from ZEPLIN-III [37] at 3,650 V/cm; solid green squares from XENON10 at 730 V/cm [38]; red markers from XENON100 [39] at 530 V/cm. The NEST prediction [33] is shown in red, green and blue for 530 V/cm, 700 V/cm (LZ baseline) and 3,650 V/cm, respectively. The green curve is used for LZ sensitivity calculations.

As the NR scintillation yield declines gently at least down to 3 keV, the ionization yield increases accordingly, as shown in Figure 3.3.3. We note that the experimental data suggest a remarkably high yield even for 1-keV recoils, with several electrons being released per interaction. As with the scintillation yield, the electric field dependence is modest.

The high ionization yield allied to the ability to detect single electrons with high efficiency is a very attractive feature of this technology: Not only

does it provide a low-threshold channel for light WIMP searches but, from a practical standpoint, it allows very high triggering efficiency (on S2) for the lowest-energy events, which are associated with very small S1 pulses.

3.3.1 Low Energy and Low Mass Sensitivity

Double-phase Xe detectors achieve the best NR energy threshold among the leading WIMP-search technologies — while maintaining discrimination and good vertex location. Of all such detectors operated so far, LUX can claim the lowest NR threshold of approximately 4 keV. WIMP masses down to ~10 GeV are directly accessible to an instrument such as LZ operating in the "normal" TPC mode, requiring one S1 pulse and one S2 pulse. A low-energy ER interaction (~1.5 keV_{ee}) is shown in Figure 3.3.1.1 — 3-D position resolution and discrimination are fully effective even at these energies.

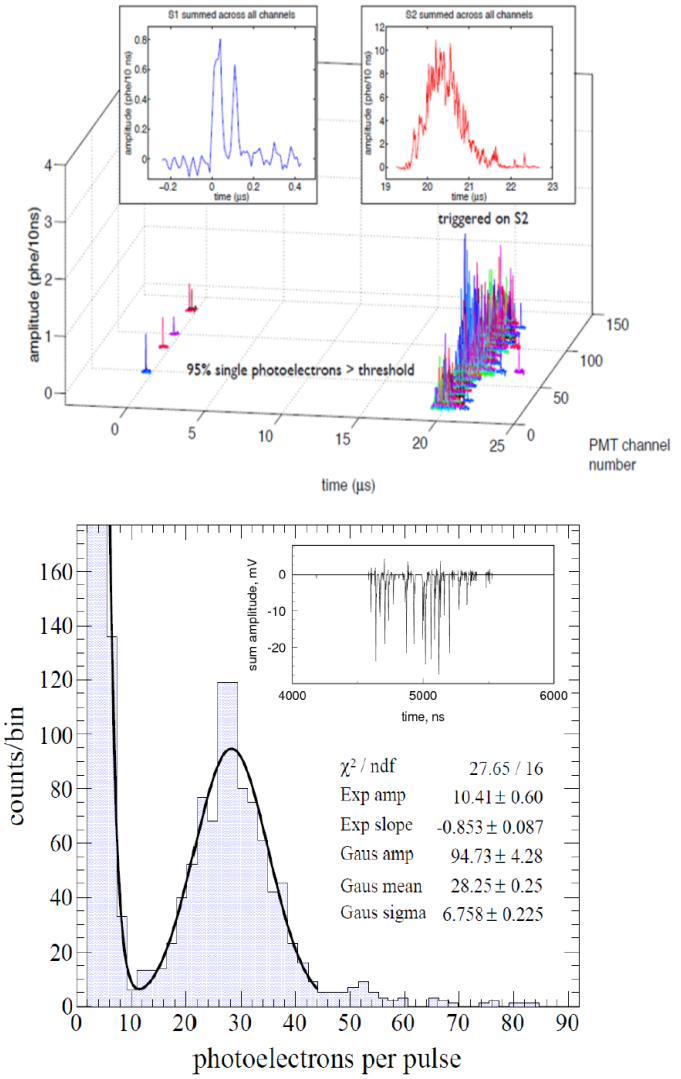

Figure 3.3.1.1. Low-energy performance of double-phase Xe detectors. Top: A 1.5-keV_{ee} electron interaction in LUX [41], showing a fivefold coincidence for S1 and the corresponding (much larger) S2 delayed by 20 µs. Bottom: Pulse size distribution of single electrons measured by electroluminescence in ZEPLIN-III, showing a mean of 28 photoelectrons per emitted electron (one such waveform is shown in inset) [18].

At the smallest NR energies (≲4 keV), it is clear that the S1 signal is often absent but S2 is still easily detectable, so that LZ can recover sensitivity in this regime by performing an "S2-only" analysis [40]. Discrimination based on S2/S1 ratio is not possible in this instance, but the detector retains the ability to reject edge events in (x,y). A more limited but still useful degree of z position reconstruction is possible based on the broadening of the S2 pulse due to longitudinal diffusion of electrons as they drift in the liquid. As a result, an S2-only search can still exploit the extremely radio-quiet inner region of the WIMP target, and place upper limits on the dark-matter scattering cross section. Naturally, a thorough understanding of backgrounds is required for this type of analysis; several background mechanisms create single S2 electrons, while the two-electron random coincidence rate might still be significant. This technique is particularly applicable to particle masses lower than about 10 GeV.

One class of NR event that inevitably will be visible below the (3-phe) S1 threshold is due to coherent elastic scattering of ^{8}B solar neutrinos off Xe nuclei. The electron counting technique (S2-only) was in fact suggested a decade ago to allow a first observation of this process [42]. Due to energy resolution broadening of the scintillation signal, some events will register both S1 and S2 — from this

and other neutrino fluxes. Despite significant interest in this signal per se, coherent neutrino-nucleus scattering is also a fundamental background for dark-matter searches, which is quantified in Chapter 4.

3.4 Electron/Nuclear Recoil Discrimination

Discrimination of ERs is key to the positive identification of a WIMP signal, both by directly reducing the effect of the dominant electronic backgrounds in the detector, and by confirming a NR origin. The physical basis for discrimination is the difference in the ratio of ionization electrons to scintillation photons that emerge from the interaction site and subsequently create the measured S2 and S1 signals, respectively. In a plot of the logarithm of S2/S1 as a function of S1, as in Figure 3.4.1, electron and nuclear recoils each form a distinct band, with NRs having a lower average charge/light ratio.

Discrimination is commonly quantified by the ER leakage past the median of the NR population (i.e., retaining a flat 50% NR acceptance). Previous values are between 99.5% in XENON10 [11] and 99.99% in ZEPLIN-III [15]. For the purpose of sensitivity calculations, we assume a baseline discrimination value of 99.5%, a conservative assumption given the performance already obtained in LUX, as discussed below.

Electron/nuclear recoil discrimination is determined by the separation of the bands as well as their widths, and in particular the "low tail" in $\log_{10}$(S2/S1) of the ER band. Remarkably, the bands are mostly Gaussian when binned in slices of S1. Some skewness was observed in the electron band in ZEPLIN-III, although this was measured with external gamma rays rather than internally dispersed sources, and at very high field [15].

The physics determining both the position of the bands and their widths has been studied and we are increasingly able to model it successfully [43]. The overall separation of the bands is mostly due to NRs producing less initial ionization and more direct excitation (leading to scintillation) than do ERs. In turn, the bandwidths depend strongly on the physics of electron-ion recombination at the interaction site. A

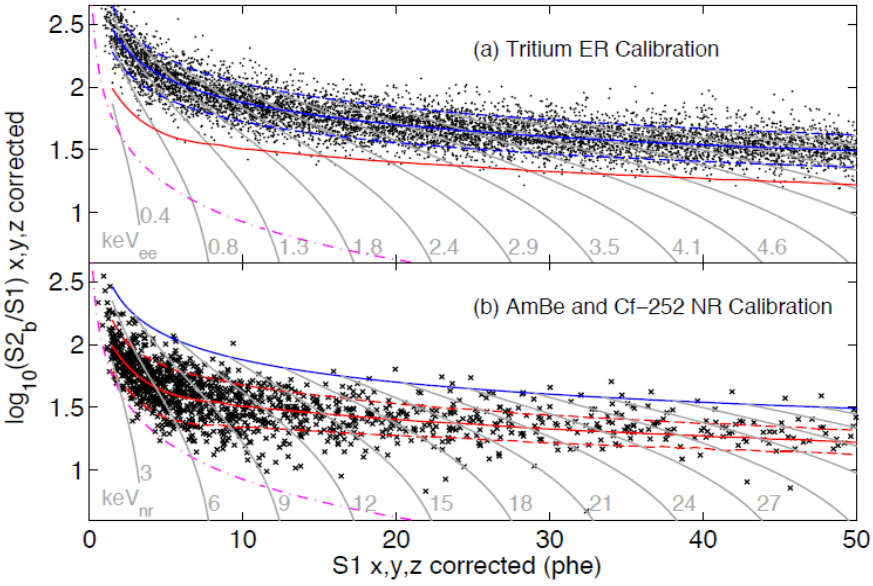

Figure 3.4.1. Discrimination parameter $\log_{10}$(S2/S1) as a function of S1 signal obtained with LUX calibration [4]. (a) ER band calibrated with beta decays from a dispersed ^{3}H source; the median is shown in blue, with 80% population contours indicated by the dashed blue lines. (b) NR band populated by elastic neutron scattering from AmBe and ^{252}Cf neutron sources; the median and 80% bandwidth are indicated in red, but in this instance they are defined via simulation to account for systematic effects present in neutron-calibration data (but not expected in a WIMP signal). The mostly vertical gray lines are contours of constant energy deposition. For more information, see Chapter 4.

recombination episode generates an excited Xe atom that de-excites through scintillation (via the Xe_2^* state). Therefore, initial ionization is either measured as charge (via S2) or light (via S1), and event-by-event fluctuations in the amount of recombination are one of the primary sources of band broadening. These fluctuations increase with recoil energy over the range of interest.

At the lowest energies, however, the distributions "flare up" due to statistical fluctuations in the S1 signal. This broadening is therefore reduced in chambers with higher light yield, improving discrimination. In fact, ER rejection in this technology is better just above threshold (~5–15 keV), where WIMP-induced recoil rates are highest, than at intermediate energies (~15–40 keV), and then improves dramatically beyond ~40 keV. The excellent ER discrimination at low energies is due in part to a decrease of recombination fluctuations, but is also caused by the curvature of both bands at low energy, as shown in Figure 3.4.1: The bands are largely *parallel* to the direction of S1 fluctuations, sharply reducing their impact on discrimination.

In addition to light collection, the drift field is also expected to affect discrimination. Although largely determined by the amount of initial ionization, the positions of the band medians have a residual dependence on the different amounts of field-dependent recombination for the two recoil species, and their separation increases at higher fields [43]. This may explain the world-best discrimination observed in ZEPLIN-III, which operated with close to 4 kV/cm drift field, and is an important driver of the LZ design. The bandwidth should, in principle, also have some field dependence, though this has not been well measured. The model developed in [43] has been incorporated in the NEST Monte Carlo package [33,30], which, as described below, has informed the sensitivity projections for this report. However, caution must be exercised when comparing values from different experiments, since instrumental effects other than electric field and light yield can impact discrimination very severely. A case in point is the degraded discrimination measured in the second science run (SSR) of ZEPLIN-III [44] relative to the first science run (FSR) [15], benchmarked essentially in the same detector and with the same software, but following upgrade of the TPC with underperforming photomultipliers.

The question of discrimination is of great important in LZ, as its dominant background is ERs from solar neutrinos. To predict the LZ sensitivity, the *electric field strength* and the *light-collection efficiency* in the WIMP target are the main ingredients required. These are key performance parameters and we motivate their choice in two separate sections below; we also describe the steps we are taking to achieve the required performance. We use these parameters in conjunction with a full Geant4 Monte Carlo simulation [45] based on the LUXSim package [46] and incorporating NEST, which we also describe briefly below.

The adopted values — a drift field of 700 V/cm and an S1 photon detection efficiency (PDE) of 7.5% — motivate an average nominal discrimination of 99.5% for a flat ER spectrum such as that from solar pp neutrinos (an ER leakage past the NR median of 1:200). This is supported by both NEST-based simulations and by XENON10 [11], which achieved that level of discrimination at similar field and light collection as proposed here. PANDA-X recorded 99.7% at 667 V/cm, for a PDE of 10.5% [47]. Significantly, LUX initially reported 99.6% discrimination at only 180 V/cm in Run 3 [4], increasing to 99.8% in a subsequent reanalysis with improved algorithms. Therefore, we are confident of reaching the 99.5% value assumed in this report.

Figure 3.4.2 shows how the discrimination generally improves for smaller S1 signals, as measured in LUX. In addition, a light-WIMP signal is not distributed symmetrically around the NR median: Upward fluctuations in S1 that cause low-energy events to be considered above a given analysis threshold also dictate that the distribution of $\log_{10}$(S2/S1) is systematically lower than the NR median, and so the acceptance for light WIMPs is higher than the 50% generally mentioned here. We will assess how this higher acceptance translates to light-WIMP sensitivity in Chapter 4.

A potential limitation to ER discrimination comes from multiply-scattered gamma rays, in which a well-measured, low-energy scatter in the active TPC is accompanied by a further interaction in a region that yields a light signal but no charge (e.g., the liquid below the cathode). If the pathology of these so-called

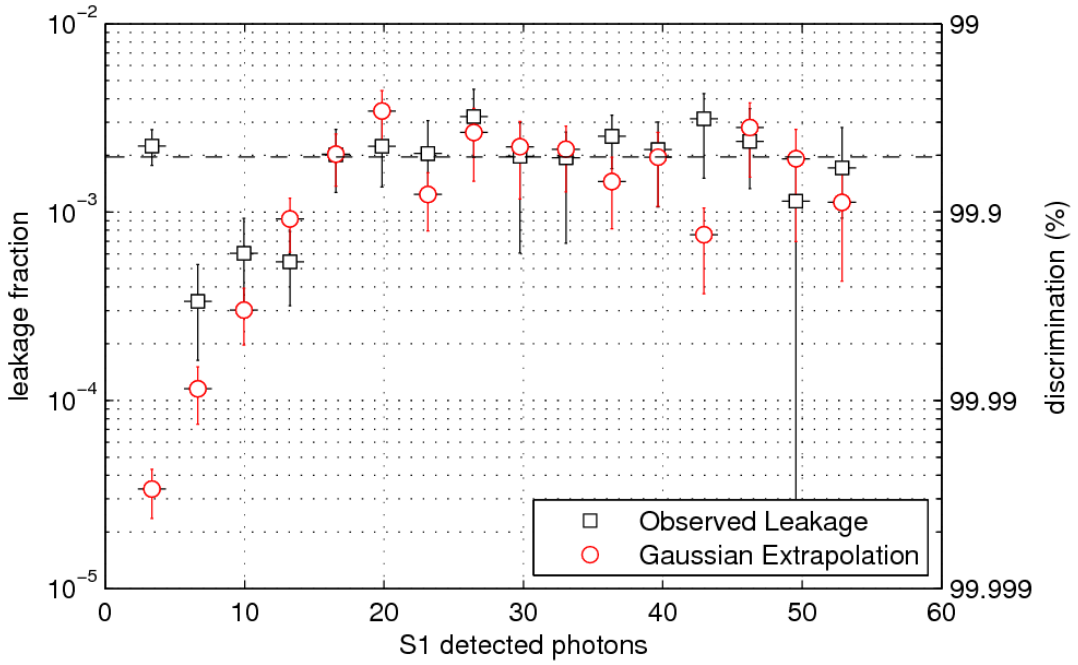

Figure 3.4.2. ER leakage fraction past the NR median line measured with tritium data in LUX. Black squares are from event counting and the red circles are from integrating the tails of Gaussian fits to the ER population. The dashed line indicates the average leakage of 0.002 (99.8% discrimination) in the S1 range 2–50 phe. The general improvement of discrimination at low energies can be clearly seen, with the exception of the very lowest S1 data point where the ER band starts to flare up due to photoelectron statistics.

"gamma-X" events is not recognized (by, for instance, the light pattern in the bottom PMT array), the result is a suppressed S2/S1 ratio, potentially mimicking a NR. Such events are subdominant in an instrument as large as LZ, where gamma-ray interactions are very rare in the fiducial volume. In addition, LZ minimizes inactive "skin" volumes by instrumenting the LXe outside of the TPC, effectively turning these potentially problematic regions into an additional veto detector. In defining a preliminary fiducial volume in Section 3.8.5, used for the sensitivity calculations presented in Chapter 4, we have assumed, rather conservatively, that events with one vertex in these regions (e.g., sub-cathode) are not vetoed. In reality, most will exhibit S1 light patterns that are strongly peaked in a single bottom-array PMT, which makes them atypical when compared with the deepest fiducial interactions and provides therefore a basis for their removal.

3.4.1 Discrimination Modeling with NEST

NEST (Noble Element Simulation Technique) provides a model for both the scintillation light and ionization charge yields of nuclear and electron recoils as a function of electric field and energy or dE/dx [33,30,32]. "NEST" refers both to a collection of microscopic models for energy deposition in noble elements and to the Monte Carlo simulation code that implements these models. NEST provides mean yields and intrinsic fluctuations due to the physics of excitation, ionization, and recombination, including both Gaussian and non-Gaussian components of the energy resolution. To properly model the discrimination of nuclear versus electron recoils, the mean S1 and S2 yields must be known, but also their variances, which are made up of the intrinsic fluctuations referred to above as well as of instrumental fluctuations and data-analysis effects.

Since discrimination is a function of electric-field strength, recoil energy, and light-collection efficiency, all of these must be modeled together to predict the baseline LZ sensitivity. To validate this methodology,

NEST was initially trained on data from the small double-phase detector from Case Western Reserve University (Xed), which yielded comprehensive data sets in terms of energy range and field sweep [43].

3.4.2 High Voltage: Results, Design, and Program

The cathode HV in LZ is an important performance parameter that will directly affect the science reach of the instrument because of its impact on ER rejection. Introduction of HV into the Xe space is challenging due to possible charge buildup and sparking, and also because high-field regions can produce unwanted electroluminescence and electron emission that blind the detector to the flashes of scintillation light produced by WIMP interactions.

The LZ *operational* and *design* voltages were determined by considering the trade-offs between dark-matter sensitivity, project cost, and risk. Between December 2012 and April 2013, a dedicated LZ Task Force of 10 engineers and scientists examined the various design proposals and critically evaluated their technical feasibility, with the scope covering the electrode grids, portions of the field cage, internal connections, and the cathode feedthrough. The Task Force recommended an operational cathode HV of 100 kV, so as to generate a 700 V/cm drift field. This should ensure an ER rejection efficiency of 99.5%, as demonstrated in XENON10 and supported by NEST (and now surpassed in LUX). The design goal for cathode HV was set at 200 kV; all subsystems will be designed to withstand this higher value to help ensure that the 100 kV operational voltage can be met with high probability.

No double-phase Xe detector developed for rare-event searches has yet been able to operate at nominal-design electric fields "as built." In the past, maximum design fields were considered that were a relatively modest factor below the onset of electroluminescence in the liquid (~400 kV/cm), as reported in the literature [48-50]. However, breakdown or some form of "electroluminescence" has invariably been observed at fields at least an order of magnitude lower than expected. The choice of a reasonable "allowable field" — to be adhered to everywhere within the LXe space — is therefore a useful concept. We surveyed several double-phase Xe chambers to determine the average fields observed at the surface of cathode wires, typically where the highest voltage gradients are located, which could be applied stably and for which this stability could be established down to single quanta of light and charge. This level of stability is essential, for example, for the cathode and gate wire grids within the TPC, although it may well be a conservative assumption for external metal surfaces.

We do not yet have a complete understanding of the breakdown mechanisms at play in previous detectors. Several hypotheses have been considered, namely ion-related, UV-related, or particulate/dust effects, as well as enhanced field emission from asperities, Xe ice layers, and oxide layers, to mention a few. This remains the focus of R&D at several LZ institutes (see Section 6.7) and was the subject of a workshop organized in part by LZ scientists in November 2014 [51]. There is considerable evidence that it is indeed possible to achieve up to 400 kV/cm in LXe, at least on some cathodic surfaces. The surface gradient on cathode wires may be a special case, as it will involve ion processes directly and with much higher density than any other electrode in the system.

We identified several examples of HV gradients achieved stably at the cathodes of several LXe experiments. In all cases, the detector operated just below the onset of instability. For example, ZEPLIN-III sustained 40–60 kV/cm in two long runs [15,44], using 100-micron stainless steel wires, and so did its prototype chambers at Imperial [52] and ITEP-Moscow [53,54]. Significantly, the Xed prototype reached a value of 220 kV/cm [55], but with different material wires (Cu-Be, 40 micron diameter). This is the only case we identified in which a significantly higher field was sustained for long periods within the liquid — but it is also the case that the total span of wire used in this chamber was small: 0.5 m, compared with 117 m for the ZEPLIN-III cathode. The XENON100 cathode voltage was limited to −16 kV for stable operation, resulting in a drift field of 0.53 kV/cm across the TPC. Higher cathode voltages resulted in additional light pulses, likely caused by field-emitted electrons and subsequent scintillation in the strong electric field near sharp features of the cathode mesh [56]. In the LUX experiment, the cathode wire grid was built from 206-micron stainless steel wire, with 5 mm wire pitch.

Table 3.4.2.1. High field regions in LZ at the operating cathode HV of 100 kV.

Electrode	Medium	Voltage Gradient	Safety Factor
Cathode wire surface	LXe	37 kV/cm	1.4
Gate wire surface	LXe	69 kV/cm	0.7
Field cage†	LXe	23 kV/cm	2.2
Cathode ring OD	LXe	34 kV/cm	1.5
Reverse field region	LXe	25 kV/cm	2.0
HV umbilical	LXe	41 kV/cm	1.2
HV cable	Polyethylene	194 kV/cm	3.0*
HV feedthrough	Epoxy	30 kV/cm	4.9‡

†Near start of vessel taper; *580 kV/cm maximum rating; ‡150 kV/cm maximum rating

During underground commissioning, light production was seen when the field at the cathode wire surface exceeded ~20 kV/cm, assuming a cylindrical wire without defects. LUX is still in operation, and it has not been determined why light was generated at such low nominal values. However, it is suspected that metal or plastic debris attached to the wire creates higher fields than would otherwise be present. This light production limited LUX to a cathode voltage of −10 kV, which resulted in a drift field of 0.18 kV/cm in its 48-cm drift region.

At the moment, we are adopting a value of 50 kV/cm as the maximum allowable field for stable operation of immersed metal surfaces throughout the LZ detector. Table 3.4.2.1 summarizes high field regions in the LZ design; our goal is to achieve safety factors of at least 2 so that we are compliant with the maximum allowable field at the full design voltage. Additional design work is needed and will be informed by our R&D results, which may lead us to make minor design modifications to some components (e.g., wire grids) or it may motivate an increase in allowable field from the 50 kV/cm considered presently — at least for some materials or surfaces. In any case, we note that LUX has already matched the discrimination assumed in LZ sensitivity calculations at much lower drift field.

Three approaches to HV delivery are being developed, all depicted in Figure 3.4.2.1. The first approach (and also the LUX baseline design) is a warm feedthrough, placed at room temperature outside the water tank. The second approach is a cold, low-radioactivity feedthrough, located at LXe temperature at the base of the cryostat [57,58]. The third approach is a Cockcroft-Walton generator, located in LXe-filled conduit within the water tank.

The warm feedthrough approach places the cathode HV insertion at the end of a long, vacuum-insulated, Xe-filled umbilical, outside the water shield at room temperature. With the dominant cable material being polyethylene, radon emanation is minimized. The outgassing properties of the polyethylene to be used in LZ have been measured and found to be acceptable from the perspective of Xe purity (see Chapter 9). With the feedthrough at room temperature and far away from the active LXe, there are no concerns about thermal contraction compromising a leak-tight seal to the Xe space, and no major constraints from feedthrough radioactivity. A feedthrough at the warm end of the umbilical allows a commercial polyethylene-insulated cable to pass from a commercial power supply, through an epoxy plug, and into the gaseous Xe. The cable then passes through the center of the umbilical and routes the HV through LXe and to a field-graded connection to the cathode. A smaller version of this feedthrough is installed in LUX, and was successfully tested up to 100 kV. A warm feedthrough prototype has already been successfully tested at Yale up to 200 kV, with the HV cable terminated in transformer oil. A more detailed description of the warm feedthrough approach may be found in Chapter 6.

The benefit of a cold feedthrough is that right up until the port on the cryostat, the HV can be delivered through a vacuum space rather than Xe. This alleviates concerns regarding radon permeation and outgassing, impurities contaminating the Xe, and complications with Xe recirculation through such conduits. It also allows commercial HV cable to be used all the way to the feedthrough, without the

additional heat flux from such cable to the liquid, and avoiding risk from gas pockets and virtual leaks. Two insulating materials are being considered: quartz and polyethylene. Challenges to this approach include reliable sealing of the feedthrough at cryogenic temperatures, field distortions that might be produced after thermal contraction, and feedthrough radioactivity.

Internal HV generation using a rectifier circuit (Cockcroft-Walton) is being investigated. This AC-DC conversion would be done in the LXe, using a stack of capacitors and diodes to shuttle charge up to a high potential. This approach avoids the difficulties of passing high voltages through Xe gas, or passing extremely high voltages through a leak-tight feedthrough. The Cockcroft-Walton approach is commonly used for reaching high voltages in Van de Graaff accelerators but, in the case of LZ, the generator must not produce excessive radioactive background, nor generate RF radiation that could compromise the PMT arrays and instrumentation electronics [59]. By spatially separating the Cockcroft-Walton generator from the TPC, both radioactive background and RF noise may be greatly mitigated. The HV must then be transported through LXe to the cathode, as in the warm or cold feedthrough approaches.

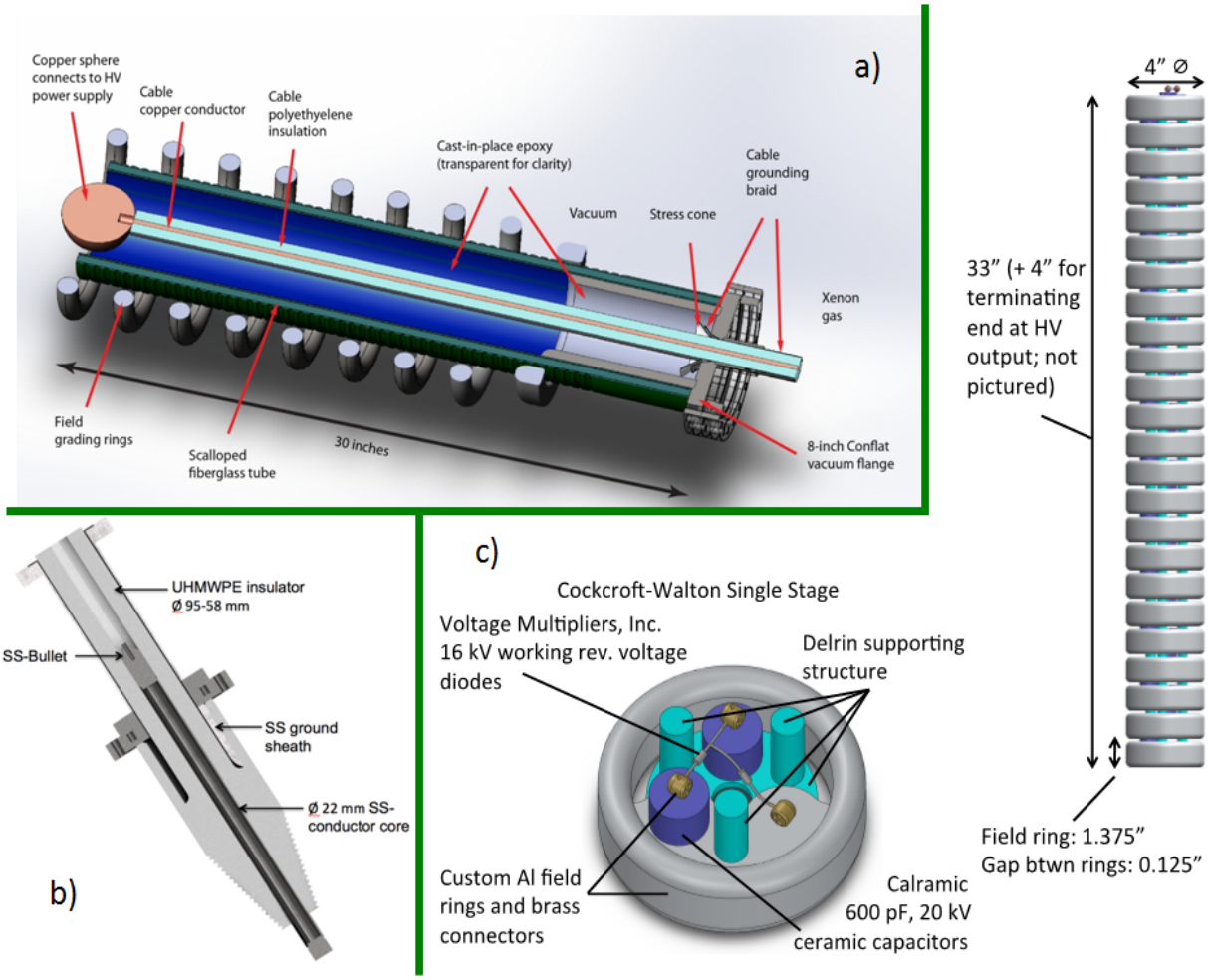

Figure 3.4.2.1. HV delivery options in LZ. (a): The warm feedthrough approach (baseline design); (b) the cold feedthrough approach; (c) the Cockcroft-Walton generator approach.

3.4.3 Light Collection: Results, Design, and Program

The energy thresholds associated with S1 and S2 are determined in each case by the microscopic light and charge yields of LXe and the light-collection efficiency of the chamber. For a given energy acceptance window, the magnitude of S1 also impacts discrimination, as highlighted above (e.g., Figure 3.4.2).

Maximizing the sensitivity of this response channel is therefore an experimental priority. Scintillation yields for electron and nuclear recoils, described in Section 3.3, depend also on energy and electric field. For reference, at the nominal LZ field we expect 470 scintillation photons to be emitted from a 10-keV electron track (47 ph/keV$_{ee}$), and 75 photons from a 10-keV NR (7.5 ph/keV). The experimental challenge is to maximize how many are recorded as photoelectrons in the PMT arrays.

In comparison, the electroluminescence yield in Xe vapor is high (typically ~1000 photons/cm per emitted electron [60], as discussed in Chapter 6); additionally, S2 light is recorded with high efficiency by the upper PMT array. This allows sub-keV$_{ee}$ detection thresholds to be easily achieved, and the sensitivity of the S2 channel is usually not a concern — in fact, single electrons emitted from the liquid can be detected straightforwardly, as mentioned previously.

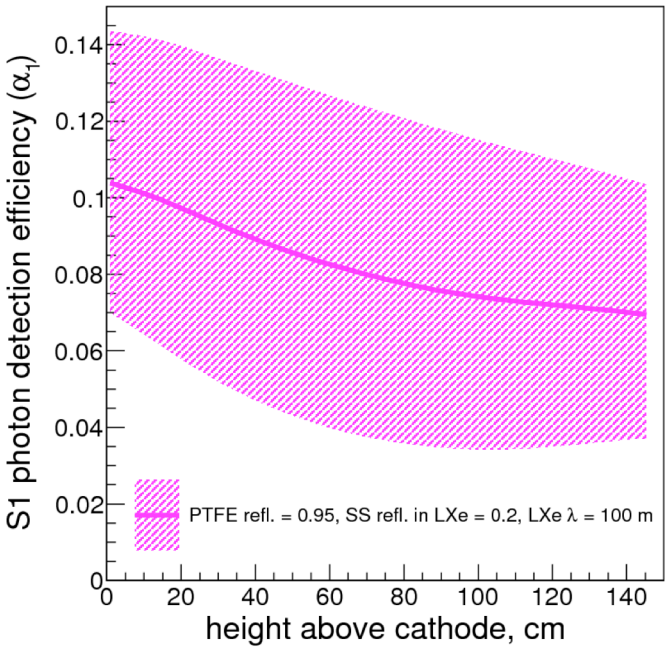

Figure 3.4.3.1. Simulated S1 photon-detection efficiency as a function of distance from the cathode for three light-collection scenarios, averaging 4.4% (lower bound), 8.3% (line), and 12.5% (upper bound). Varied parameters are the PTFE and grid reflectivities and the photon absorption length; the number of PMTs (488) and their QE at 178 nm (25%) is the same in all cases. The baseline assumed for sensitivity calculations is α_1=7.5%, with 5.0% and 10% also assessed to represent pessimistic and optimistic scenarios.

The LXe scintillation emission is centered at 178 nm, with FWHM = 14 nm [61]. Light from electroluminescence in Xe vapor has a similar spectrum, but not quite identical [12]. Wavelength shifting is not required since the Xe luminescence spectrum is compatible with quartz-windowed photomultipliers. The basic optical properties of LXe are established: The refractive index for scintillation light is n = 1.67 [62], which is well matched to that of quartz (n = 1.57). This allows good optical coupling to the PMTs immersed in the liquid phase. The Rayleigh scattering length is 30–50 cm (see [12] and references therein), which must be considered in optical simulations.

The key issue is then to maximize the S1 photon-detection efficiency, α_1, which measures the fraction of emitted scintillation photons that generate detected photoelectrons. The main factors affecting α_1 in LZ are: (1) the VUV reflectivity of internal surfaces made from PTFE; (2) the photon absorption length in the liquid bulk; (3) the geometric transparency and reflectivity of all grids; (4) the PMT photocathode coverage fraction; and (5) the PMT optical performance.

Below we discuss briefly these parameters and how they translate into the three light-collection scenarios assumed for LZ in this report; these are illustrated in Figure 3.4.3.1. Optical simulations for the baseline justify a volume-averaged α_1 = 7.5%, and we adopt also pessimistic and optimistic combinations of parameters that support α_1 =5% and 10%, respectively.

The phototube specification and array layout are addressed in Chapter 6; here we assume tightly packed top and bottom arrays of 3-inch tubes (top and bottom arrays with 247 and 241 units, respectively), with average QE = 25%. This conservative QE matches the manufacturer specification and allows for double-photoelectron emission observed in some photocathodes at these wavelengths (and not captured by the

QE specification). This is an important issue that we are presently investigating in the LUX and LZ PMTs [63]. We use the lower value in all three optical simulation scenarios, although typical QEs reported by the manufacturer for LXe scintillation are more like 30%.

The photon absorption length in the bulk LXe depends on the purity of the liquid with respect to trace amounts of contaminants with absorption bands overlapping the LXe scintillation spectrum, mostly H_2O and O_2. For our tight purity requirements for those electronegative species (0.1 ppb, see Chapter 9), a value $l \sim 100$ m is reasonable (see Figure 15 in [12]), but we vary this parameter from 10 m to 1,000 m for the other scenarios.

The five grids in the LZ TPC all affect light collection through obscuration and wire reflectivity and, in a chamber where other sources of optical extinction have been minimized, these grids can have a significant effect in the light yield, especially those immersed in the liquid. Our baseline assumption is 20%, varied to fully absorptive or to 50% reflective for the other two scenarios.

Finally, the last and perhaps most important optical parameter is the reflector used in constructing the TPC. Based on a decade of experience, PTFE is indeed the best reflector for LXe scintillation, and also for properties other than optical: The manufacturing process yields very radiopure material (~ppt in U/Th); it has good mechanical properties (despite about 1.2% thermal contraction to LXe temperatures); and outgassing rates are relatively low (see Chapter 9). Optically, reflectivities of at least 90–95% have been reported in LXe chambers [64,65,41], and evidence from LUX suggests even higher values. Unlike metallic coatings such as aluminum, also a good VUV reflector [66], the optical properties of PTFE will not degrade during the lifetime of the experiment.

The VUV reflectivity of PTFE is a critical parameter in these detectors and for this reason we initiated a study of its optical properties at LIP-Coimbra. In vacuum, the reflectivity depends strongly on the manufacturing process and surface finish; best results were obtained with molded PTFE after polishing [67]. It is also known that optical properties differ for low- and high-density versions of the fluoropolymer [68]. However, we found also that the properties of the PTFE-LXe interface are not well predicted by straightforward modification of the optical models derived from vacuum measurements with Xe scintillation: An average hemispherical reflectance of 90% is predicted [67,69], which is consistently lower than measured in the liquid. A dedicated test chamber was constructed for this purpose, which involves a small LXe cell with lateral walls made from the PTFE under test, photomultiplier readout from the top, and an α-particle source at the bottom. The chamber is filled progressively and the resulting response is fitted by a five-parameter optical model that returns the reflectivity of the liquid and gas interfaces, among others. Preliminary results for the same PTFE as used in LUX are confirming 97% hemispherical reflectance when immersed in the liquid; this is shown in Figure 3.4.3.2. This result is in good agreement with that derived by comparing LUX data with optical simulations from LUXSim. Candidate materials (different types, finishes, and

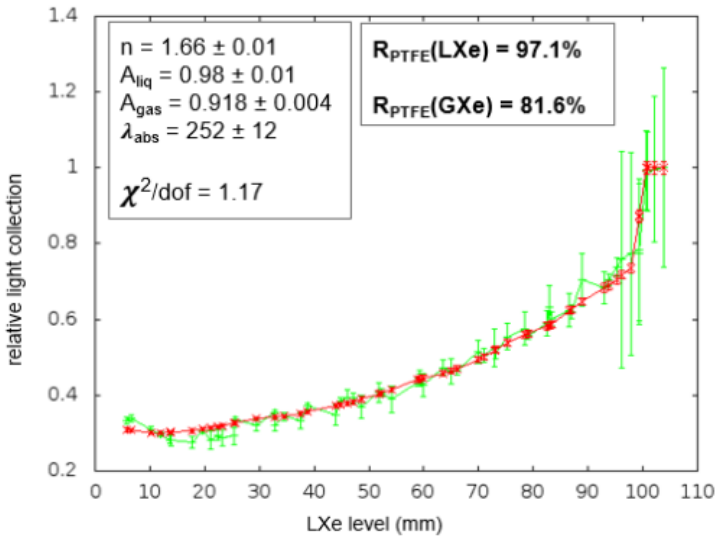

Figure 3.4.3.2. Measurement (green) and simulation-derived fit (red) of the total hemispherical reflectance of the PTFE/LXe interface in a LXe scintillation cell. The PTFE sample under study is the material used in LUX, and it makes up the lateral walls of the test chamber.

manufacturers) can be tested in this way before procurement for construction. We adopt a somewhat conservative reflectivity of 95% in our optical simulations for the baseline, with 90% for the pessimistic and 99% for the optimistic scenarios.

To reduce the dead volume around the active LXe, as well as outgassing and potential backgrounds, it is desirable to minimize the thickness of the PTFE walls of the TPC and skin detectors. A lower limit is established by the transmittance of PTFE to Xe scintillation light, and the need for optical isolation between the TPC and skin regions as well as between these and any dead regions containing LXe. The transmittance of the PTFE used in LUX was measured as a function of thickness and for different wavelengths: Xe gas scintillation (178 nm) as well as 255, 340, and 470 nm. Results for Xe scintillation light show a transmittance <0.1% for 1.5 mm PTFE thickness, but rising significantly to as much as 10% for 5 mm in the case of blue light (470 nm).

The baseline α_1 of 7.5% translates to an S1 response of 4.7 phe/keV at zero field for ^{57}Co gamma rays (a traditional measure of light yield in LXe chambers) — cf. 8.8 phe/keV in LUX [4], 6.6 in XENON10 [11,17], 5.0 in ZEPLIN-III [15], 4.3 in XENON100 [56], and 1.1 in ZEPLIN-II [9]. According to NEST, the corresponding NR energy threshold is approximately 6 keV for a 3-phe coincidence requirement, which we adopt for our sensitivity estimates. We note that a lower, twofold coincidence may be possible (as in LUX Run 3) that would lower the 6 keV threshold.

3.5 Outer Detector Systems

A WIMP scatter would deposit a few keV in the central volume of the LXe TPC, with no simultaneous energy deposit in surrounding materials. Radioactivity neutrons, which can fake WIMP interactions when they scatter elastically, are likely to interact again either within the TPC or nearby, and so it is broadly desirable to replace as much of the neighboring material as possible with additional radiation detectors. It also helps to minimize intervening material between the active LXe in the TPC and any such ancillary detectors, namely by decreasing the thickness of the field-cage and of the cryostat vessels. Active material surrounding the central LXe volume also permits assessment of the local radioactivity environment, and thus to infer additional information on the backgrounds in the WIMP search region. A persuasive WIMP discovery will require excellent understanding of all background sources, which is best done through the characterization of those sources in situ.

The LZ apparatus will feature two distinct regions where active material surrounds the LZ TPC. The first is a "skin" of LXe, formed by liquid between the field cage and the inner vessel of the cryostat. The second is surrounding detectors of liquid scintillator (LS), which is doped with a small amount of gadolinium, to enhance its capability for neutron detection. We envisage a threshold of 100–200 keV_{ee} for both systems, with the gadolinium-doped LS detecting neutrons more effectively and the skin detector performing best for internal gamma rays.

3.5.1 Xenon Skin Veto

The lateral skin region consists of an unavoidable 4–8 cm of LXe between the outer boundary of the field cage and the inner boundary of the cryostat. An even thicker LXe region exists below the bottom PMT array. It is highly desirable to read out scintillation light generated in these regions for two main reasons: Besides constituting anti-coincidence detectors in their own right, they will also tag external LXe interactions where VUV photons can leak into the TPC and fake S1 light there. Our approach has been to maximize the optical isolation between active and inactive LXe volumes as far as practicable, and to instrument as much passive LXe as possible. The sensitivity to deposited energy in the skin will be far less than that of the central Xe TPC and, naturally, no ionization can be detected.

To get reasonable utility for vetoing gamma rays, the threshold should be a small fraction of the typical energy of an environmental gamma. A threshold of about 100 keV_{ee} is adequate to detect Compton recoils from MeV gamma rays from radiogenic backgrounds. The skin detector will have low sensitivity for

neutron detection via elastic scattering due to the mismatch in mass between neutrons and Xe nuclei, but inelastic neutron interactions can be still detected.

The LXe skin veto has some advantages over the outer detector for gamma detection in that some gamma rays do not penetrate the various vessels all the way to the LS. Our design studies indicate that a threshold of 100 keV_{ee} can be reached if the walls of the skin volumes are sufficiently reflective, and as long as the photocathode coverage is sufficient. Approximately 120 1-inch Hamamatsu R8520 PMTs, split into top and bottom arrays, will monitor the cylindrical shell between the sides of the TPC and the cryostat wall, with a threshold of three photoelectrons providing a 100 keV_{ee} energy threshold. In the bottom region below the TPC, a further 60 1-inch PMTs provide a similar sensitivity.

Should the threshold be worse than 100 keV_{ee}, there will be additional ER background in the LZ fiducial mass. For 300 keV_{ee}, the rate of ERs in the 5.6-tonne LZ fiducial mass roughly doubles, but would still be an order of magnitude below the ER rate from solar neutrinos. The skin detector is further described in Section 6.7.

3.5.2 Scintillator Outer Detector

The goal of the outer detector is to surround the LZ cryostat with a near-hermetic gamma-ray and neutron anticoincidence system. Much of the challenge is of a practical nature: Deep underground, the safety of combustible LS solvents is a prominent concern. Fabricating the large (~5-m-tall) tanks for underground deployment successfully and economically are other important considerations.

LZ will employ linear alkyl benzene (LAB), an LS solvent developed by the reactor neutrino community in the past decade [70]. The flash point of LAB is >120^{o}C, exceeding that of diesel fuel (commonly used underground for backup generators). Small quantities of a standard fluor and wavelength shifter will be added to the solvent to provide the scintillation signal. A PMT system located in the water space outside of the clear acrylic tanks containing the LS will view this scintillation light.

To enhance neutron detection, 0.1% by weight of natural gadolinium will be dissolved in the LAB with a chelating agent to form Gd-loaded LS, or GdLS. Two isotopes of Gd, ^{155}Gd and ^{157}Gd, have neutron-capture cross sections that are 61 and 254 kilobarn, respectively. Each of these isotopes constitutes about 15% of natural Gd and, at 0.1% concentration by weight, capture on Gd is about 1 order of magnitude more probable than is capture on hydrogen.

A neutron that can cause a Xe NR in the same energy range as the recoil from a WIMP will have an energy between about 0.5 and 5 MeV. The source of most of these neutrons will be from the (α,n) process from material around the edges of the Xe, and their energy spectrum will be toward the low end of this interval. A dangerous neutron will enter the LXe TPC and then scatter back out after one interaction. Many of those neutrons will traverse the intervening material and then thermalize and capture in the Gd in the GdLS. The length scale for thermalization and capture is a few centimeters and the typical capture time is ~30 μs, which is small compared with the 670 μs maximum drift time of the TPC.

After capture on Gd, a total energy of about 8 MeV is emitted as a burst of several gamma rays, which then interact in the LS (or the skin, or the TPC). This large energy release separates neutron captures from the gamma rays from natural radioactivity, which die out above 3 MeV. The thickness of the GdLS is determined by the gamma scattering length, which is ~25 cm. The thickness of the GdLS layer is 75 cm, or three scattering lengths. For a fraction of gamma rays that deposit energy in the central LXe TPC, the outer detector system also functions as a gamma-ray veto, for those that propagate through the LXe skin and cryostat; these share the same detection requirements as the capture gammas. To achieve good efficiency as a gamma-ray veto, we need a threshold to Compton electrons near 100 keV_{ee}.

In reactor neutrino experiments, typically a single acrylic cylinder contains the Gd-loaded scintillator. Transport logistics preclude this solution for LZ, and instead segmentation of the volume into nine smaller tanks that can be transported through the shafts and drifts that lead to the Davis Cavern is the adopted solution. To enhance light collection, the outer surface of the LZ cryostat will be affixed with a

diffuse white reflective layer of Tyvek© to reflect light into the 8-inch Hamamatsu R5912 PMTs that will surround the tanks. The 600-μm multilayer Tyvek© we plan to use has a reflectivity in excess of 95%.

The PMT collecting power must be sufficient to achieve a 100 keV_{ee} threshold. Our preliminary studies indicate that, by covering the cryostat in Tyvek© and employing another reflective cylinder outside of the PMT system, the collecting power of 120 8-inch PMTs is sufficient to achieve the required threshold.

The GdLS tanks will be surrounded by ultrapure water, and the distance to the water-space PMT system that detects the LS scintillation light must be sufficient to attenuate gamma rays from PMT radioactivity (these are not low-background models). A distance of 80 cm from the scintillator tanks to the PMTs reduces the rate from this source to less than 5 Hz.

The tightest specifications on radioactive impurities in the GdLS arise from considerations of deadtime caused by the outer detector system. Asking that the false veto probability not exceed 1% over 4 neutron capture times results in requirements of <1.7 ppt U, <3.2 ppt Th, <0.6 ppt ^{40}K, and $<2 \times 10^{-18}$ g/g in ^{14}C. While LAB itself generally exceeds this requirement, the additives must be purified somewhat more completely than has been achieved in the reactor neutrino experiments. The purity achieved by the Borexino Collaboration greatly exceeds the LZ requirements for U/Th/K. Borexino demonstrated a ^{14}C impurity slightly above that needed for LZ [71]. Chapter 7 details the implementation and performance of the outer detector more fully.

3.6 Internal Calibration with Dispersed Sources

The physics of self-shielding allows LZ to achieve its unprecedented sensitivity by reducing the rate of gamma-ray scatters in the energy range of interest to a level of secondary importance. Arguably, this is the central feature of the LZ detector design. Conversely, the same effect presents a challenge for a calibration program based solely on external gamma sources such as ^{137}Cs. Such a calibration campaign may be useful for monitoring the edges of the detector and calibrating at higher energies, but will be of limited utility for probing the detector response to low energy interactions in the fiducial volume.

To take full advantage of a monolithic dark-matter detector such as LZ, it is necessary to implement internal calibration methods that can temporarily defeat the self-shielding effect. The development of such sources has been accomplished through a global R&D effort with major contributions from LZ scientists (e.g., [72]), and LUX is the first working experiment to rely primarily on internal calibration sources as the workhorses of its calibration campaign.

Two internal sources have been successfully deployed within LUX: ^{83m}Kr, a source of 9.4 keV and 32.1 keV conversion electrons, separated in time by an average of 154 ns; and tritium (^{3}H), a β^- emitter with a *Q*-value of 18.6 keV.

The radioisotope ^{83m}Kr has a half-life of 1.8 hours, and is ideal for calibrating the spatial response of LUX to S1 and S2, for monitoring the free-electron lifetime, and for setting the energy scale in both response channels. It has also been useful for imaging the fluid flow in the LUX detector. (However, note that the scintillation yield of the second [9.4 keV] electron is affected by the ionization left behind by the first transition [31].) LUX deployed ^{83m}Kr on average about twice per week throughout the physics running period, and these calibration data sets have been the primary method for monitoring the detector response during its first WIMP search run. LZ will capitalize on this success.

While the ^{83m}Kr conversion electrons are ideal sources for routine monitoring of S1 and S2, they are less useful for measuring the ER discrimination factor in the energy range of interest (<6.5 keV_{ee}). Tritium, however, emits a beta particle with a maximum energy of 18.6 keV and a most probable energy of only 3 keV, allowing the discrimination efficiency to be determined over the full WIMP-search energy range, including probing the detector threshold at low energy. Tritium has been deployed with good results in LUX in the chemical form of tritiated methane (CH_3T). The primary challenge presented by tritium is its long half-life (12.3 years), which necessitates that the source must be removed by active purification. The

effectiveness of the purification was carefully studied by LUX in bench-top tests, and those good results culminated in the decision to proceed with a CH_3T injection in the summer of 2013. The result of this injection was shown previously in Figure 3.4.1: This confirms that the ER band is uniformly populated down to the lowest energies, with a source of ERs that allows calibration of the intrinsic bandwidth — as opposed to gamma rays, which interact resonantly with bound atomic electrons. The experience gained through the LUX calibration program is driving the design and implementation of the LZ effort.

3.7 Xenon Purity for Detector Performance

The fluid nature of LXe provides an opportunity to manipulate the purity of the LZ target material. The previous section describes how this allows internal calibration sources to be temporarily introduced into the LXe. This section considers how the purity can be maximized for low-background physics running. We consider two classes of impurities: the radioactive noble gases ^{85}Kr and ^{222}Rn — although the latter is addressed fully only in Chapter 12 — and electronegative contaminants such as oxygen and water.

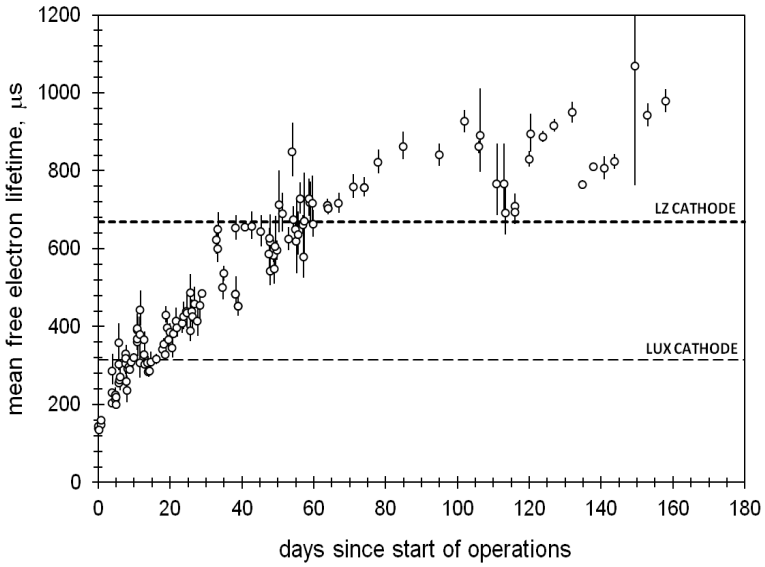

Figure 3.7.1. Evolution of the mean free electron lifetime in LUX from the start of underground operations. The electronegative purity required to observe signals from the LZ cathode (~670 μs for the 147-cm long TPC) has already been achieved in LUX.

Electronegative impurities are introduced during operations by the outgassing of detector materials, and they must be continuously suppressed to the level of ~0.1 ppb by the purification system to ensure good charge and photon transport. Previous detectors such as ZEPLIN-III achieved this through clean construction techniques with low-outgassing materials (i.e., no plastics), which allowed these systems to maintain purity without recirculation [73]. In larger detectors such as LUX, the need to utilize large volumes of PTFE for the reasons outlined above demands active recirculation in the gas phase. The efficient removal of electronegative contaminants is made possible by purification technology developed for the semiconductor industry. The central elements of this technology are a heated zirconium getter for the removal of non-noble species, UHV-compatible plumbing and instrumentation, and a gas-circulation pump.

Despite the availability of this technology, until recently the achievement of good electronegative purity in a LXe TPC was considered a significant technical challenge. What was lacking was an economical and sensitive monitoring technique to allow the purification technology to be fully exploited. While free electron lifetime monitors for LXe were developed over 20 years ago, these devices cannot identify individual impurity species, are insensitive to noble gas impurities, and provide little guidance on the origin of any impurities.

In the past few years, however, LZ scientists have developed a mass spectrometry method that allows most electronegative and noble gas impurities to be individually monitored in real time [24]. Most crucially, the method provided, for the first time, information on the impurity source. For example, the presence of an air leak introduces N_2, O_2, and Ar in a characteristic ratio, while a large excess of N_2 is a

signature of a saturated purifier. Outgassing, on the other hand, leads to a uniform rate of increase of all common impurity species.

LZ scientists have gained experience with the mass spectrometry method by applying it not only to LUX, but also to the EXO-200 $0\nu\beta\beta$-decay experiment [74]. Both experiments achieved their purity goals with relative ease due in part to the effectiveness of this program, and this valuable experience can be brought to bear on LZ. We have learned, for example, that vendor-supplied Xe is often relatively pure of electronegatives; that zirconium getters are effective for Xe purification but that their performance degrades at higher gas flow rates; and that purifier performance improves at elevated temperature. This experience is of direct relevance for the design of the LZ purification system. This experience is bearing fruit in LUX, where electron lifetimes of the order of 1 ms have been demonstrated, as shown in Figure 3.7.1. This is already sufficient to drift charge from interactions near the LZ cathode.

An additional benefit is that the method is sensitive not only to electronegatives but also to trace quantities of noble gas impurities, which is of critical importance for control of krypton. Krypton is a particularly dangerous impurity for LZ because of the presence of the beta emitter ^{85}Kr. This isotope, whose abundance at present is $\sim 2 \times 10^{-11}$ (^{85}Kr/^{nat}Kr), presents the leading purification challenge for LZ because its noble nature makes it impervious to the zirconium getter technology. Vendor-supplied Xe typically contains about 100 ppb of ^{nat}Kr, which, if left untreated, would give rise to an ^{85}Kr beta decay rate of 29 mBq per kilogram of Xe.

Previous experiments had difficulty achieving both their free electron lifetime and krypton-removal goals. These tasks are made more difficult by a lack of tools to monitor the performance of krypton-removal systems and an inability to identify and isolate leaks during detector operation. On the other hand, by applying advanced mass spectrometry methods, LUX was able to identify, isolate, and correct small problems with its krypton-removal system; confirm that its average krypton concentration was suitable prior to physics running; and has continuously monitored O_2, N_2, Ar, and Kr during physics operations to ensure that no leaks are present. This led directly to a successful WIMP search run for LUX.

LZ will capitalize on the success of EXO-200 and LUX by integrating sensitive monitoring into its Xe handling program from the time of Xe procurement until the conclusion of the experiment. In addition, because the origin of impurities is now understood to be primarily due to outgassing, a comprehensive purification plan can be developed and implemented to ensure that LZ achieves its performance goals. In fact, we have already carried out an extensive materials outgassing screening program to aid in developing such a plan. This allows us to develop an outgassing budget for the experiment and to design an appropriate purification system to mitigate it.

While sensitive impurity monitoring will lay the groundwork for the LZ Xe purification program, the heart of the program will be krypton removal using the chromatographic technique developed at Case Western by LZ scientists [23]. This program has been successfully applied to LUX and will be scaled up in mass-throughput by a factor of 10 for LZ. The krypton concentration goal is 0.02 ppt (g/g), a factor of 200 below the LUX goal. In parallel, the krypton detection limit of the mass spectrometry method will be improved more than tenfold from the currently demonstrated value of ~0.3 ppt (g/g). The ultimate source of krypton impurities in LZ will be the outgassing of detector materials, which we can control through careful materials selection and through our outgassing plan.

Similarly, ^{222}Rn must be controlled by limiting the emanation sources within the detector and the gas system via a careful screening program. In fact, the need to limit radon and krypton in the LZ Xe will be a driving consideration in the choice of key Xe system components such as the gas-recirculation pump. More generally, the materials-screening program must work hand-in-hand with the purification effort, as the detector materials are the ultimate irreducible source of all classes of impurities.

3.8 Dominant Backgrounds

LZ has a clear background-control strategy with optimal exploitation of self-shielding to pursue an unprecedented science reach. These are the most salient features of this strategy: (1) underground operation within an instrumented water tank to mitigate cosmogenic backgrounds; (2) deployment of a target mass large enough to self-shield external radioactivity backgrounds, working in combination with outer, anticoincidence detectors; (3) construction from low-activity materials and purification of the target medium to render intrinsic backgrounds subdominant; and (4) rejection of the remaining ER backgrounds by S2/S1 discrimination.

The dominant radioactive backgrounds come from the Xe-space PMTs and their bases, field cage structures including the PTFE reflectors, and the cryostat vessels. Our goal is to self-shield those sources over the first few centimeters of active liquid and thereby be sensitive to a population of ERs caused by elastic scattering of solar pp neutrinos — which can be further discriminated by their S2/S1 ratio. An irreducible but very small background of NRs will also arise from coherent neutrino-nucleus scattering. To achieve this, we must render negligible any intrinsic ER backgrounds contained within the Xe itself, with ^{85}Kr, ^{39}Ar, and Rn progeny being a particular challenge. Electron recoils caused by the 2νββ decay of ^{136}Xe, now confirmed by the EXO-200 [75] and KamLAND-Zen [76] experiments, are subdominant below about 20 keV$_{ee}$. Cosmogenic (muon-induced) backgrounds are not significant during operation due to the tagging capability of the instrumented water tank and the scintillator veto, but cosmogenic activation of detector materials prior to deployment (including the Xe) must be addressed.

We describe briefly some of these background categories here (radioactivity external to the TPC, intrinsic contamination of the LXe, and cosmogenic backgrounds), as these are important LZ sensitivity drivers, but we postpone a full discussion on their mitigation to Chapter 12. Neutrino backgrounds, which determine the LZ sensitivity to first order, are explored further in Chapter 4. The solar pp neutrino scattering rate of 0.8×10^{-5} events/kg/day/keV$_{ee}$ is the benchmark against which other rates are assessed.

3.8.1 Backgrounds from Material Radioactivity

Radioactivity backgrounds have limited nearly all dark-matter experiments so far and, in spite of the power of self-shielding, we are not complacent in addressing them in LZ. They impact the thickness of the sacrificial layer of LXe that shields the fiducial mass, and they may cause rare-event topologies that may be of consequence (from random coincidences, atypical surface interactions, or Cherenkov emission in PMT glasses, for example). It is important, therefore, to minimize the rate of α, β, and γ activity around the active volume, as well as neutron production from spontaneous fission of ^{238}U and from (α,n) reactions. In addition, the rate and spatial distribution of such backgrounds must be well characterized to build an accurate background model for the experiment. The LZ background model is derived from a high-fidelity simulation of the experiment in the LUXSim framework mentioned previously, which was successfully used for the LUX background model [77].

All materials to be used in LZ will be subject to stringent constraints as part of the comprehensive screening campaign described in Chapter 12, with 10% of the solar pp neutrino scattering rate and a maximum of ~0.2 NRs at 50% signal acceptance being the target for the total contribution from material radioactivity within the fiducial volume. The dominant rates come from the various PMT systems and the LZ cryostat, based on the large masses and close proximity to the active region of the detector. Table 3.8.1.1 summarizes contamination and count rates from neutron and gamma-ray emission expected from detector materials and other backgrounds, which are discussed in greater detail in Chapter12.

The PMTs chosen for the LZ TPC are Hamamatsu R11410s, which have achieved very low radioactivity values; LZ scientists have been involved in a long campaign to establish their performance for dark-matter experiments, working actively with the manufacturer to enable this [21]. The PTFE required to fabricate the TPC field cage, skin reflectors, and other internal components may also be an important source of neutron emission from the bulk material. We use upper limits on the contamination measured

Table 3.8.1.1. Summary of backgrounds in LZ, showing radioactivity levels for some dominant components, their neutron emission rates, and the number of counts expected in 1,000 live days in an indicative 5.6-tonne fiducial mass between 1.5–6.5 keVee (ER) and 6–30 keV (NR). A comprehensive list can be found in Table 12.2.2.

Item	Mass kg	U mBq/kg	Th mBq/kg	^{60}Co mBq/kg	^{40}K mBq/kg	n/yr	ER cts	NR cts
R11410 PMTs	93.7	2.7	2.0	3.9	62.1	373	1.24	0.20
R11410 bases	2.7	74.6	29.1	3.6	109.2	77	0.17	0.03
Cryostat vessels	2,140	0.09	0.23	≈0	0.54	213	0.86	0.02
OD PMTs	122	1,507	1,065	≈0	3,900	20,850	0.08	0.02
Other components	-	-	-	-	-	602	9.5	0.05
Total components							11.9	0.32
Dispersed radionuclides (Rn, Kr, Ar)							54.8	-
^{136}Xe 2νββ							53.8	-
Neutrinos (ν-e, ν-A)							271	0.5
Total events							391.5	0.82
WIMP background events (99.5% ER discrimination, 50% NR acceptance)							1.96	0.41
Total ER+NR background events							2.37	

by EXO-200 in calculating its impact [78]. The cryostat is another dominant component, mostly owing to its large mass. For the titanium baseline design (2,140 kg), the total neutron emission rate is estimated at 0.6 n/day based on recent titanium samples procured for LZ. As a result of a 2-year material search campaign, we were able to find titanium with U/Th contamination, which is a factor of 2 lower than that used in LUX [22] as explained in Chapter 8.

3.8.2 Surface Plating of Radon Progeny

The noble gas radon consists solely of radioactive isotopes, of which four are found in nature: ^{222}Rn and ^{218}Rn produced in the ^{238}U decay chain, ^{220}Rn from the ^{232}Th decay chain, and ^{219}Rn from the ^{228}Ac series. As a result of its chemical inertness, radon exhibits long diffusion lengths in solids. ^{222}Rn is the most stable isotope ($T_{1/2}$ = 3.82 days), and is present in air at levels of about ten to hundreds of Bq/m^3. Charged radon progeny — especially metallic species such as ^{218}Po — plate out onto macroscopic surfaces that are exposed to radon-laden air. A fraction will deposit and even implant into material surfaces during detector construction or installation [79].

Backgrounds from surface beta and gamma radioactivity, as well as recoiling nuclei (e.g., ^{206}Pb from the alpha decay of ^{210}Po), are largely mitigated by short half-lives and the self-shielding of LXe. However, α-particles released in the decay chain, particularly from ^{210}Po — a granddaughter of the long-lived ^{210}Pb ($T_{1/2}$ = 22.3 years) — result in neutron emission following (α,n) reactions. This is problematic for TPC materials with large (α,n) yields such as PTFE (10^{-5} n/α, due to the presence of fluorine). Additionally, because PTFE is produced in granular form before being sintered in molds, plate-out poses further risk because surface contamination of the granular form becomes bulk contamination when the granules are poured into molds.

A second concern relates to our ability to correctly reconstruct surface interaction at the TPC inner walls, since the imperfect reconstruction of these events leads to a background population leaking radially toward the fiducial volume [4,9]. This concern drives the design of the top PMT array and places tight requirements on the plate-out of radon progeny on the TPC walls (see Section 6.5.3).

Controls to mitigate background from radon plate-out will include limiting the exposure of detector parts to radon-rich air; monitoring from point of production through transport and storage in Rn-proof materials; and employing surface cleaning techniques, such that neutron emission is negligible relative to material radioactivity from bulk uranium and thorium contamination.

3.8.3 Intrinsic Backgrounds

We are confident that our challenging goals for intrinsic radioactive contamination from ^{85}Kr and ^{222}Rn can be met with the Xe-purification techniques described in Chapter 9, coupled with the radon emanation screening of Xe-wetted materials described in Chapter 12. We note that most of these backgrounds can be estimated with low systematic uncertainty. In addition to direct sampling, the ^{85}Kr β^- decay spectrum is well understood and the decay rate can be measured during operation with delayed $\beta-\gamma$ coincidences.

Other delayed coincidence techniques as well as α spectroscopy allow precise estimation of radon-induced backgrounds. In fact, it is possible to follow dynamically the spatial distribution of these decays throughout the detector, which was done very successfully in LUX [80]. The two main concerns in this instance are a "weak" naked beta decay from ^{214}Pb in the bulk of the TPC (E_{max} = 1,019 keV, BR = 11%), and the possibility of gamma-ray escape for peripheral events from the dominant ^{214}Pb decay modes.

Our goal is to control each of these two backgrounds to <10% of the solar pp neutrino rate, limiting the ^{222}Rn activity to 0.67 mBq and the krypton concentration to 0.02 ppt (g/g). In a more conservative scenario, we allow the sum of these two components to match the ER background from pp neutrinos.

Trace quantities of argon are also a concern due to β-emitting ^{39}Ar, with a 269-year half-life and 565 keV endpoint energy. This background is constrained to be less than 10% of ^{85}Kr, resulting in a specification of 4.5×10^{-10} (g/g) or 2.6 μBq. The Kr-removal system, which also removes Ar, should easily achieve this.

3.8.4 Cosmogenic Backgrounds

A rock overburden of 4,300 mwe above the Davis Cavern at SURF reduces the muon flux by a factor of 3.7×10^6 relative to the surface [81]. Muons crossing the water tank are readily detected via Cherenkov emission, and any coincident energy deposition in LZ is similarly easily identified. However, muon-induced neutron production through spallation, secondary spallation, or photonuclear interactions by photons from muon-induced EM showers in high-Z materials may generate background [82,83]. The total muon-induced neutron flux at SURF from the surrounding rock is calculated to be 0.54×10^{-9} n/cm^2/s, with approximately half of this flux coming from neutrons above 10 MeV, and some 10% from energies above 100 MeV [84]. This neutron rate is considerably lower than that from internal component radioactivity.

Muon-induced neutrons generated in the water shield produce a similarly low rate, despite the several hundred tonnes of target mass, due to the low atomic number of water and consequent low neutron yield (~2.5×10^{-4} n/μ/(g/cm^2)), translating to a production rate of order 10^{-9} n/kg/s). The water itself attenuates the flux on the cryostat to ~0.2 n/day, a small contribution compared with that from the cryostat itself.

Cosmogenic activation — radioisotopes production within materials, largely through spallation reactions of fast nucleons from cosmic rays while on the Earth's surface — can present electromagnetic background in LZ. ^{46}Sc produced in the titanium cryostat decays through emission of 889 keV and 1120 keV gamma rays (with $T_{1/2}$ = 84 days). Cosmogenic ^{60}Co ($T_{1/2}$ = 5.3 years) in copper components will produce gamma rays of 1,173 keV and 1,332 keV.

Activation of the Xe itself during storage or transport generates several radionuclides, some of which are important, especially in the first few months of operation. Tritium ($T_{1/2}$ = 12.3 years and production rate of ~15/kg/day at the Earth's surface [85]) was previously a concern; however, this is effectively removed through purification during operation. Production of Xe radioisotopes, such as ^{127}Xe ($T_{1/2}$ = 36.4 days), ^{129m}Xe ($T_{1/2}$ = 8.9 days), and ^{131m}Xe ($T_{1/2}$ = 11.9 days), are more problematic, as they cannot be mitigated

through self-shielding or purification. In particular, atomic de-excitation of the 2s and 3s shells in ^{127}Xe generates 5.2 and ≤1.2 keV energy deposits, respectively, which are an important background in the WIMP search energy region for certain event topologies [4]. Since ^{127}Xe is produced efficiently through neutron resonance capture, shielding against thermal neutrons is desirable even when stored underground. Furthermore, these backgrounds soon reach negligible levels once underground operation starts.

3.8.5 Fiducialization

To assess the impact of all sources of background in LZ, it is sensible to define a fiducial volume, even if only approximately at this stage. A rigorous definition will involve sophisticated statistical analyses that take into account their measured spatial distribution. However, for the purpose at hand as well as for reasons of design and engineering, it is sensible to know the approximate location of such a volume.

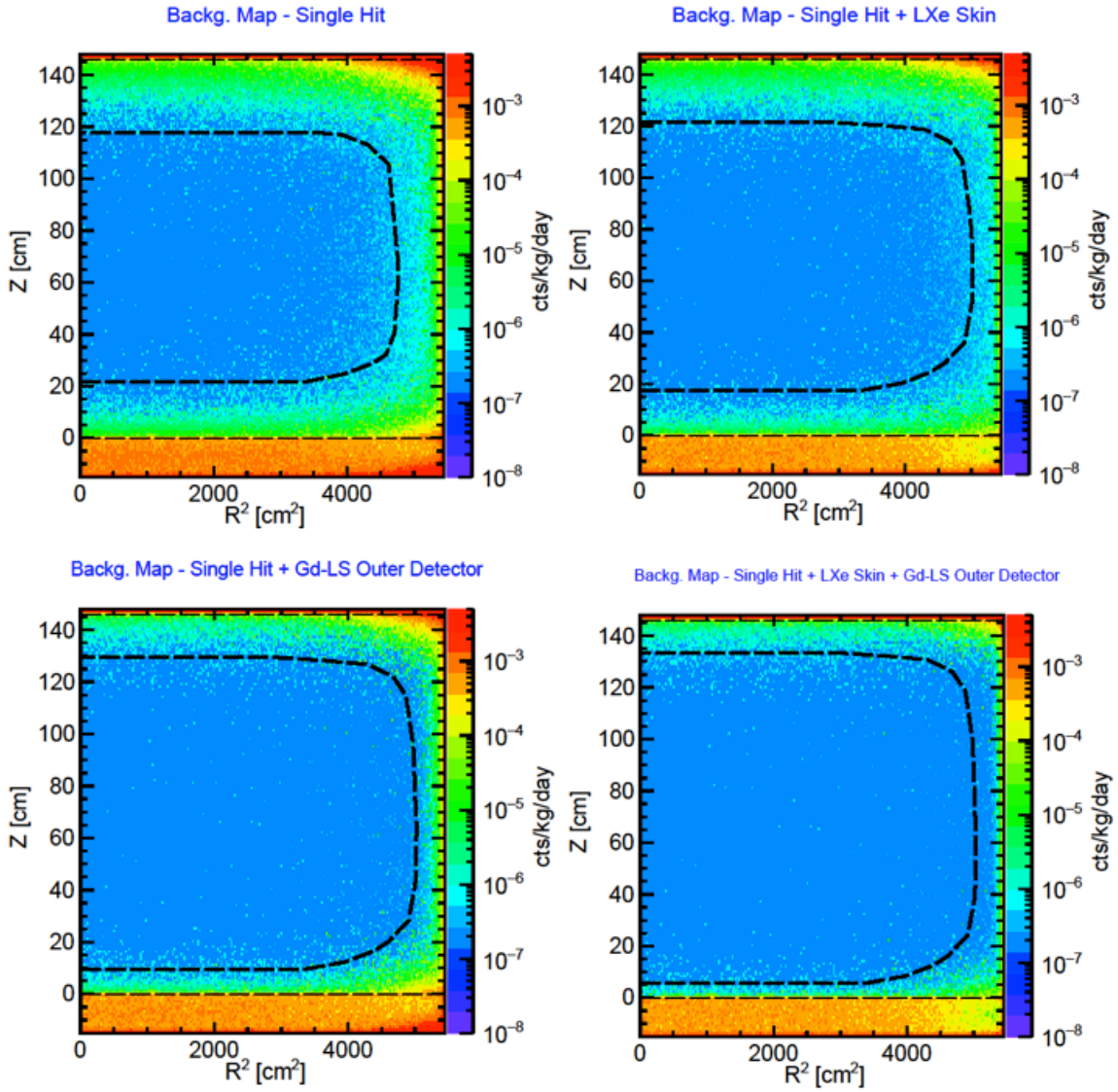

Figure 3.8.5.1. Total NR background plus ER leakage from sources external to the LXe in the TPC, counted over a 6–30 keV acceptance region; a discrimination efficiency of 99.5% is applied to ERs from gamma rays and solar pp neutrinos. Top left: Single scatters only, no vetoing by the anti-coincidence systems. Top right: Adding LXe skin only. Bottom left: Adding GdLS outer detector only. Bottom right: Adding the combination of both vetoes. In each panel, approximate fiducial contours are shown in the black dashed line and weigh 3.3, 4.2, 5.1, and 5.6 tonnes, respectively.

Two main factors determine how far the fiducial boundary should lie from the lateral TPC walls. The prime consideration is to ensure a sufficiently thick layer of LXe to self-shield against the external radioactivity backgrounds; this is related to the mean attenuation length for those particles: Figure 3.2.2 confirmed that ~2 cm of liquid decreases the gamma-ray background tenfold, and as much as ~6 cm is needed to mitigate neutrons by the same factor. However, the outer detector is very efficient for neutron tagging, which brings these two requirements closer together.

Secondly, it is essential that the reconstructed (x,y) positions of low-energy interactions occurring near the TPC walls do not "leak" into the fiducial volume. As mentioned above (and discussed in Chapter 6) interactions from radon progeny plating the lateral PTFE are of particular concern: These can generate events with very small S2 signals due to trapping of charge drifting too close to the PTFE. If allied with poor position resolution, this can constitute a very challenging background [9]. In the vertical direction, only the former consideration arises. We point out that the reverse field region below the cathode will provide much of the required self-shielding (>14 cm), whereas at the top, the small thickness of liquid above the gate (0.5 cm) will have a limited impact.

Figure 3.8.5.1 shows the simulated background rate from material radioactivity in the WIMP region of interest (6–30 keV) as a function of radius squared and height above the cathode grid. Nuclear and electron recoil backgrounds were combined, with 50% acceptance applied to the former and 99.5% discrimination applied to the latter. The neutrino contributions listed in Table 3.8.1.1 were included. TPC events with additional sub-cathode vertices (gamma-X) are not rejected, making this a conservative assessment (see brief discussion in Section 3.4). In each panel, we show the number of background counts per kg per day, with the dashed black line indicating the position of an approximate fiducial volume. This is drawn so as to constrain the ER background from radioactivity to one-tenth of the solar pp neutrino rate, and separately to constrain the NR background from radioactivity to ~0.2 events in 1,000 days. The four panels are for single hit interactions with no further vetoes, then adding either the skin or the outer detector, then combining the two anti-coincidence systems. In the first case (top left), with no additional vetoes applied, the fiducial cut is 15 cm away from the wall, retaining a fiducial mass of 3.3 tonnes.

The final panel illustrates what can be gained by our dual "veto" strategy. Using the combination of skin and outer detectors (both with 100 keV_{ee} threshold) improves the estimated fiducial mass to 5.6 tonnes. In this instance, the lateral cut is 4 cm away from the wall, which is also a reasonable distance to allow good position reconstruction for wall events and to avoid electric field non-uniformity near the field-cage surface. The total estimated background count in this fiducial volume in a 1,000-day data set is ~2.4 events, as indicated in Table 3.8.1.1.

Chapter 3 References

[1] P. Belli, R. Bernabei, S. D'Angelo, A. Incicchitti, and D. Prosperi, Nuovo Cim. **A103**, 767 (1990).

[2] G. J. Davies, W. G. Jones, J. D. Davies, J. D. Lewin, and P. F. Smith, Phys. Lett. **B320**, 395 (1994).

[3] P. Benetti *et al.*, Nucl. Instrum. Meth **A327**, 203 (1993).

[4] D. S. Akerib *et al.* (LUX), Phys. Rev. Lett. **112**, 091303 (2014), arXiv:1310.8214 [astro-ph].

[5] G. J. Alner *et al.* (ZEPLIN-I), Astropart. Phys. **23**, 444 (2005).

[6] Z. Ahmed *et al.* (CDMS-II), Phys. Rev. Lett. **102**, 011301 (2009), arXiv:0802.3530 [astro-ph]; R. Agnese *et al.* (SuperCDMS), Phys. Rev. Lett. **112**, 241302 (2014), arXiv:1402.7137 [hep-ex].

[7] P. Benetti *et al.* (WARP), Astropart. Phys. **28**, 495 (2008), arXiv:astro-ph/0701286 [astro-ph].

[8] P. Agnes *et al.* (DarkSide), Phys. Lett. **B743**, 456 (2015), arXiv:1410.0653 [astro-ph].

[9] G. J. Alner *et al.* (ZEPLIN-II), Astropart. Phys. **28**, 287 (2007), arXiv:astro-ph/0701858 [astro-ph].

[10] D. Yu. Akimov *et al.* (ZEPLIN-III), Astropart. Phys. **27**, 46 (2007), arXiv:astro-ph/0605500 [astro-ph].

[11] E. Aprile *et al.* (XENON10), Astropart. Phys. **34**, 679 (2011), arXiv:1001.2834 [astro-ph].

[12] V. Chepel and H. Araújo, J. Instrum. **8**, R04001 (2013), arXiv:1207.2292 [physics.ins-det].

[13] E. Aprile and T. Doke, Rev. Mod. Phys. **82**, 2053 (2010), arXiv:0910.4956 [physics.ins-det].

[14] V. N. Solovov *et al.* (ZEPLIN-III), in *Nuclear Science Symposium and Medical Imaging Conference (NSS/MIC), 2011 IEEE* (2011) pp. 1226–1233, *Position Reconstruction in a Dual Phase Xenon Scintillation Detector*; V. N. Solovov *et al.* (ZEPLIN-III), IEEE Trans. Nucl. Sci. **59**, 3286 (2012), arXiv:1112.1481 [physics.ins-det].

[15] V. N. Lebedenko *et al.* (ZEPLIN-III), Phys. Rev. **D80**, 052010 (2009), arXiv:0812.1150 [astro-ph].

[16] B. Edwards *et al.* (ZEPLIN-II), Astropart. Phys. **30**, 54 (2008), arXiv:0708.0768 [physics.ins-det].

[17] P. F. Sorensen, *A Position-Sensitive Liquid Xenon Time-Projection Chamber for Direct Detection of Dark Matter: The XENON10 Experiment*, Ph.D. thesis, Brown U., Phys. Dept. (2008).

[18] E. Santos *et al.* (ZEPLIN-III), J. High Energy Phys. **2011**, 115 (2011), arXiv:1110.3056 [physics.ins-det].

[19] A. Benoit *et al.* (EDELWEISS), Phys. Lett. **B513**, 15 (2001), arXiv:astro-ph/0106094 [astro-ph].

[20] D. Abrams *et al.* (CDMS), Phys. Rev. **D66**, 122003 (2002), arXiv:astro-ph/0203500 [astro-ph].

[21] D. S. Akerib *et al.* (LUX), Nucl. Instrum. Meth. **A703**, 1 (2013), arXiv:1205.2272 [physics.ins-det].

[22] D. S. Akerib *et al.* (LUX), "Radio-assay of Titanium samples for the LUX Experiment," (2011), arXiv:1112.1376 [physics.ins-det].

[23] A. I. Bolozdynya, P. P. Brusov, T. Shutt, C. E. Dahl, and J. Kwong, in *Proceedings of the 11th Symposium on Radiation Measurements and Applications Ann Arbor, MI, USA 23–26 May 2006*, Nucl. Instrum. Meth., Vol. **A579** (2007) pp. 50–53, *A chromatographic system for removal of radioactive ^{85}Kr from xenon*.

[24] D. S. Leonard, A. Dobi, C. Hall, L. Kaufman, T. Langford, S. Slutsky, and Y.-R. Yen, Nucl. Instrum. Meth. **A621**, 678 (2010), arXiv:1002.2742 [physics.ins-det].

[25] M. B. Chadwick *et al.*, Nuclear Data Sheets **112**, 2887 (2011), special issue on ENDF/B-VII.1 library.

[26] M. J. Berger *et al.*, XCOM: Photon Cross Section Database (version 1.5) (2010), National Institute of Standards and Technology, 100 Bureau Drive, Stop 1070, Gaithersburg, MD 20899-1070.

[27] E. Aprile *et al.* (XENON100), Phys. Rev. Lett. **109**, 181301 (2012), arXiv:1207.5988 [astro-ph].

[28] H. Uchida *et al.* (XMASS-I), PTEP **2014**, 063C01 (2014), arXiv:1401.4737 [astro-ph].

[29] B. A. Dolgoshein, V. A. Lebedenko, and B. U. Rodionov, JETP Lett. **11**, 351 (1970).

[30] M. Szydagis, A. Fyhrie, D. Thorngren, and M. Tripathi (NEST), *Proceedings, LIght Detection In Noble Elements (LIDINE2013)*, J. Instrum. **8**, C10003 (2013), arXiv:1307.6601 [physics.ins-det].

[31] E. Aprile *et al.*, Phys. Rev. **D86**, 112004 (2012), arXiv:1209.3658 [astro-ph].

[32] L. Baudis, H. Dujmovic, C. Geis, A. James, A. Kish, A. Manalaysay, T. M. Undagoitia, and M. Schumann, Phys. Rev. **D87**, 115015 (2013), arXiv:1303.6891 [astro-ph].

[33] B. Lenardo, K. Kazkaz, M. Szydagis, and M. Tripathi (NEST), "A Global Analysis of Light and Charge Yields in Liquid Xenon," (2014), [submitted to IEEE Trans. Nucl. Sci.], arXiv:1412.4417 [astro-ph].

[34] M. Szydagis, N. Barry, K. Kazkaz, J. Mock, D. Stolp, M. Sweany, M. Tripathi, S. Uvarov, N. Walsh, and M. Woods (NEST), J. Instrum. **6**, P10002 (2011), arXiv:1106.1613 [physics.ins-det].

[35] A. Manzur, A. Curioni, L. Kastens, D. N. McKinsey, K. Ni, and T. Wongjirad, Phys. Rev. **C81**, 025808 (2010), arXiv:0909.1063 [physics.ins-det].

[36] G. Plante, E. Aprile, R. Budnik, B. Choi, K. L. Giboni, L. W. Goetzke, R. F. Lang, K. E. Lim, and A. J. Melgarejo Fernandez, Phys. Rev. **C84**, 045805 (2011), arXiv:1104.2587 [nucl-ex].

[37] M. Horn *et al.* (ZEPLIN-III), Phys. Lett. **B705**, 471 (2011), arXiv:1106.0694 [physics.ins-det].

[38] P. Sorensen *et al.*, in *Proceedings, 8th International Workshop on The Identification of Dark Matter (IDM 2010)*, Proc. of Science, Vol. **IDM2010** (2011) p. 017, *Lowering the low-energy threshold of xenon detectors*, arXiv:1011.6439 [astro-ph].

[39] E. Aprile *et al.* (XENON100), Phys. Rev. **D88**, 012006 (2013), arXiv:1304.1427 [astro-ph].

[40] J. Angle *et al.* (XENON10), Phys. Rev. Lett. **107**, 051301 (2011), [Erratum: Phys. Rev. Lett. 110, 249901 (2013)], arXiv:1104.3088 [astro-ph].

[41] D. S. Akerib *et al.* (LUX), Astropart. Phys. **45**, 34 (2013), arXiv:1210.4569 [astro-ph].

[42] C. Hagmann and A. Bernstein, in *Proceedings, 2003 IEEE Nuclear Science Symposium, Room-Temperature Semiconductor Detector Workshop, and Symposium on Nuclear Power Systems (2003 NSS/RTSD/SNPS)*, IEEE Trans. Nucl. Sci., Vol. **51** (2004) pp. 2151–2155, *Two-phase emission detector for measuring coherent neutrino-nucleus scattering*, arXiv:nucl-ex/0411004 [nucl-ex].

[43] C. E. Dahl, *The physics of background discrimination in liquid xenon, and first results from Xenon10 in the hunt for WIMP dark matter*, Ph.D. thesis, Princeton U. (2009).

[44] D. Yu. Akimov *et al.* (ZEPLIN-III), Phys. Lett. **B709**, 14 (2012), arXiv:1110.4769 [astro-ph].

[45] S. Agostinelli *et al.* (GEANT4), Nucl. Instrum. Meth. **A506**, 250 (2003).

[46] D. S. Akerib *et al.* (LUX), Nucl. Instrum. Meth. **A675**, 63 (2012), arXiv:1111.2074 [physics.data-an].

[47] M. Xiao *et al.* (PandaX-I), Sci. China Phys. Mech. Astron. **57**, 2024 (2014), arXiv:1408.5114 [hep-ex].

[48] S. E. Derenzo, T. S. Mast, H. Zaklad, and R. A. Muller, Phys. Rev. **A9**, 2582 (1974).

[49] K. Masuda, S. Takasu, T. Doke, T. Takahashi, A. Nakamoto, S. Kubota, and E. Shibamura, Nucl. Instrum. Meth **160**, 247 (1979).

[50] E. Aprile, H. Contreras, L. W. Goetzke, A. J. Melgarejo Fernandez, M. Messina, J. Naganoma, G. Plante, A. Rizzo, P. Shagin, and R. Wall, J. Instrum. **9**, P11012 (2014), arXiv:1408.6206 [physics.ins-det].

[51] E. Bernard, C. H. Faham, T. M. Ito, B. Lundberg, M. Messina, F. Monrabal, S. P. Pereverzev, F. Resnati, P. C. Rowson, M. Soderberg, T. Strauss, A. Tomas, J. Va'vra, and H. Wang, in *High Voltage in Noble Liquids for High Energy Physics*, J. Instrum., Vol. **9**, edited by B. Rebel and C. Hall (2014) p. T08004, arXiv:1403.3613 [physics.ins-det].

[52] A. S. Howard (UK Dark Matter), in *Nonaccelerator new physics. Proceedings, 4th International Conference, NANP '03, Dubna, Russia, June 23-28, 2003*, Phys. Atom. Nucl., Vol. **67** (2004) pp. 2032–2040, *Dark matter searches by the Boulby Collaboration and liquid xenon prototype development*.

[53] A. A. Burenkov, D. Yu. Akimov, Yu. L. Grishkin, A. G. Kovalenko, V. N. Lebedenko, V. N. Solovov, V. N. Stekhanov, F. Neves, and T. J. Sumner, Phys. Atom. Nucl. **72**, 653 (2009), [Yad. Fiz.72,693(2009)].

[54] D. Yu. Akimov *et al.*, Instrum. Exp. Tech. **55**, 423 (2012), [Prib. Tekh. Eksp.2012,no.4,6(2012)].

[55] T. Shutt, A. Bolozdynya, P. Brusov, C. E. Dahl, and J. Kwong, in *Dark Matter 2006. Proceedings of the 7th UCLA Symposium on Sources and Detection of Dark Matter and Dark Energy in the Universe*, Nucl. Phys. Proc. Suppl., Vol. **173** (2007) pp. 160–163, *Performance and Fundamental Processes at Low Energy in a Two-Phase Liquid Xenon Dark Matter Detector*, arXiv:astro-ph/0608137 [astro-ph].

[56] E. Aprile *et al.* (XENON100), Astropart. Phys. **35**, 573 (2012), arXiv:1107.2155 [astro-ph].

[57] E. Bernard, C. H. Faham, T. M. Ito, B. Lundberg, M. Messina, F. Monrabal, S. P. Pereverzev, F. Resnati, P. C. Rowson, M. Soderberg, T. Strauss, A. Tomas, J. Va'vra, and H. Wang, in *High Voltage in Noble Liquids for High Energy Physics*, J. Instrum., Vol. **9**, edited by B. Rebel and C. Hall (2014) p. T08004, pp. 23-26, arXiv:1403.3613 [physics.ins-det].

[58] A. Teymourian, Y. Meng, E. Pantic, and H. Wang, B. Am. Phys. Soc. **58** (2013), *Development and Testing of a High Voltage Feedthrough for Noble Liquid TPCs*.

[59] A. Badertscher *et al.*, J. Instrum. **7**, P08026 (2012), arXiv:1204.3530 [physics.ins-det].

[60] A. Fonseca, R. Meleiro, V. Chepel, A. Pereira, V. Solovov, and M. Lopes, in *Nuclear Science Symposium Conference Record, 2004 IEEE*, Vol. **1** (2004) pp. 572–576, *Study of secondary scintillation in xenon vapour*.

[61] J. Jortner, L. Meyer, S. A. Rice, and E. G. Wilson, J. Chem. Phys. **42**, 4250 (1965).

[62] V. N. Solovov, V. Chepel, M. I. Lopes, and A. Hitachi, Nucl. Instrum. Meth. **A516**, 462 (2004), arXiv:physics/0307044 [physics.optics].

[63] C. H. Faham, V. M. Gehman, A. Currie, A. Dobi, P. Sorensen, and R. J. Gaitskell, J. Instrum. **10**, P09010 (2015), arXiv:1506.08748 [physics.ins-det].

[64] M. Yamashita, T. Doke, K. Kawasaki, J. Kikuchi, and S. Suzuki, Nucl. Instrum. Meth **535**, 692 (2004).

[65] V. Chepel, F. Neves, A. Solovov, M. I. Lopes, J. Pinto da Cunha, P. Mendes, A. Lindote, C. P. Silva, R. Ferreira Marques, and A. J. P. L. Policarpo, in *Nuclear Science Symposium Conference Record, 2004 IEEE*, Vol. **1** (2004) pp. 422–426, *Performance of a chamber for studying the liquid xenon response to nuclear recoils*, arXiv:physics/0501036 [physics]; F. Neves, V. Chepel, A. Solovov, M. I. Lopes, J. Pinto da Cunha, P. Mendes, A. Lindote, C. P. Silva, R. Ferreira Marques, and A. J. P. L. Policarpo, IEEE Trans. Nucl. Sci. **52**, 2793 (2005).

[66] R. P. Madden, and L. R. Canfield and G. Hass, J. Opt. Soc. Am. **53**, 620 (1963).

[67] C. Silva, J. Pinto da Cunha, A. Pereira, M. I. Lopes, V. Chepel, V. Solovov, and F. Neves, Nucl. Instrum. Meth. **A619**, 59 (2010), arXiv:0910.1058 [physics.ins-det].

[68] B. K. Tsai, D. W. Allen, L. M. Hanssen, B. Wilthan, and J. Zeng, in *Reflection, Scattering, and Diffraction from Surfaces, 11-12 August 2008, San Diego, California, USA*, Proc. SPIE, Vol. **7065** (2008) p. 70650Y, *A comparison of optical properties between high density and low density sintered PTFE*.

[69] C. F. P. da Silva, *Study of the reflectance distributions of fluoropolymers and other rough surfaces with interest to scintillation detectors*, Ph.D. thesis, Universidade de Coimbra, Faculdade de Ciências e Tecnologia (2009).

[70] F. P. An *et al.* (Daya Bay), Nucl. Instrum. Meth. **A685**, 78 (2012), arXiv:1202.6181 [physics.ins-det]; X. Guo *et al.* (Daya Bay), "A Precision measurement of the neutrino mixing angle θ_{13} using reactor antineutrinos at Daya-Bay," (2007), proposal, arXiv:hep-ex/0701029 [hep-ex].

[71] G. Alimonti *et al.* (Borexino), Nucl. Instrum. Meth. **A600**, 568 (2009), arXiv:0806.2400 [physics.ins-det].

[72] L. W. Kastens, S. B. Cahn, A. Manzur, and D. N. McKinsey, Phys. Rev. **C80**, 045809 (2009), arXiv:0905.1766 [physics.ins-det].

[73] P. Majewski *et al.* (ZEPLIN-III), in *Position sensitive detectors. Proceedings, 9th International Conference, PSD9, Aberystwyth, UK, September 12-16, 2011*, J. Instrum. **7**, C03044 (2012), arXiv:1112.0080 [physics.ins-det].

[74] A. Dobi *et al.*, Nucl. Instrum. Meth. **A675**, 40 (2012), arXiv:1109.1046 [physics.ins-det].

[75] N. Ackerman *et al.* (EXO-200), Phys. Rev. Lett. **107**, 212501 (2011), arXiv:1108.4193 [nucl-ex].

[76] A. Gando *et al.* (KamLAND-Zen), Phys. Rev. **C85**, 045504 (2012), arXiv:1201.4664 [hep-ex].

[77] D. S. Akerib *et al.* (LUX), Astropart. Phys. **62**, 33 (2015), arXiv:1403.1299 [astro-ph].

[78] D. S. Leonard *et al.*, Nucl. Instrum. Meth. **A591**, 490 (2008), arXiv:0709.4524 [physics.ins-det].

[79] V. E. Guiseppe, S. R. Elliott, A. Hime, K. Rielage, and S. Westerdale, in *Topical Workshop on Low Radioactivity Techniques: LRT-2010*, AIP Conf. Proc., Vol. **1338**, edited by R. Ford (2011) pp. 95–100, *A Radon Progeny Deposition Model*, Conference Presentation, arXiv:1101.0126 [nucl-ex].

[80] A. W. Bradley, *LUX Thermosyphon Cryogenics and Radon-Related Backgrounds for the First WIMP Result*, Ph.D. thesis, Case Western Reserve U. (2014).

[81] D.-M. Mei, C. Zhang, K. Thomas, and F. Gray, Astropart. Phys. **34**, 33 (2010), arXiv:0912.0211 [nucl-ex].

[82] L. Reichhart *et al.* (ZEPLIN-III), Astropart. Phys. **47**, 67 (2013), arXiv:1302.4275 [physics.ins-det].

[83] F. E. Gray, C. Ruybal, J. Totushek, D.-M. Mei, K. Thomas, and C. Zhang, Nucl. Instrum. Meth. **A638**, 63 (2011), arXiv:1007.1921 [nucl-ex].

[84] D.-M. Mei and A. Hime, Phys. Rev. **D73**, 053004 (2006), arXiv:astro-ph/0512125 [astro-ph].

[85] D.-M. Mei, Z.-B. Yin, and S. R. Elliott, Astropart. Phys. **31**, 417 (2009), arXiv:0903.2273 [nucl-ex].